



Multi-model assessment of the late-winter extra-tropical response to El Niño and La Niña

Bianca Mezzina¹ · Javier García-Serrano^{1,2} · Ileana Bladé² · Froila M. Palmeiro² · Lauriane Batté³ · Constantin Ardilouze³ · Marianna Benassi⁴ · Silvio Gualdi^{4,5}

Received: 10 April 2020 / Accepted: 7 August 2020
© The Author(s) 2020

Abstract

El Niño–Southern Oscillation (ENSO) is known to affect the Northern Hemisphere tropospheric circulation in late-winter (January–March), but whether El Niño and La Niña lead to symmetric impacts and with the same underlying dynamics remains unclear, particularly in the North Atlantic. Three state-of-the-art atmospheric models forced by symmetric anomalous sea surface temperature (SST) patterns, mimicking strong ENSO events, are used to robustly diagnose symmetries and asymmetries in the extra-tropical ENSO response. Asymmetries arise in the sea-level pressure (SLP) response over the North Pacific and North Atlantic, as the response to La Niña tends to be weaker and shifted westward with respect to that of El Niño. The difference in amplitude can be traced back to the distinct energy available for the two ENSO phases associated with the non-linear diabatic heating response to the total SST field. The longitudinal shift is embedded into the large-scale Rossby wave train triggered from the tropical Pacific, as its anomalies in the upper troposphere show a similar westward displacement in La Niña compared to El Niño. To fully explain this shift, the response in tropical convection and the related anomalous upper-level divergence have to be considered together with the climatological vorticity gradient of the subtropical jet, i.e. diagnosing the tropical Rossby wave source. In the North Atlantic, the ENSO-forced SLP signal is a well-known dipole between middle and high latitudes, different from the North Atlantic Oscillation, whose asymmetry is not indicative of distinct mechanisms driving the teleconnection for El Niño and La Niña.

Keywords ENSO · NAO · Atmospheric teleconnections · Climate modeling

1 Introduction

The teleconnection of El Niño–Southern Oscillation (ENSO) to the North Atlantic–European (NAE) sector is a long-explored topic that, however, is still controversial in several aspects. A first cornerstone on the topic—and starting point of this study—was set in a review by Brönnimann (2007), who concluded that a robust ENSO signal exists over the NAE region in late winter (January to March, JFM): a dipole in sea-level pressure (SLP) with centers over the mid-latitude and high-latitude North Atlantic (see “Appendix 1”). He referred to this signal as “canonical”, though acknowledging the existence of other, “non-canonical” views. While Brönnimann (2007) described this canonical pattern as “close to symmetric” for El Niño and La Niña, recent studies revisiting the topic and targeting linearities/non-linearities deliver contradictory results, with some reporting a symmetric signal (e.g. Deser et al. 2017; Ayarzagüena et al. 2018; Weinberger et al. 2019) and others claiming asymmetry (e.g.

Electronic supplementary material The online version of this article (<https://doi.org/10.1007/s00382-020-05415-y>) contains supplementary material, which is available to authorized users.

✉ Bianca Mezzina
bianca.mezzina@bsc.es

- ¹ Barcelona Supercomputing Center (BSC), Barcelona, Spain
- ² Group of Meteorology, Universitat de Barcelona (UB), Barcelona, Spain
- ³ CNRM, Université de Toulouse, Météo-France, CNRS, Toulouse, France
- ⁴ Climate Simulations and Predictions Division, Fondazione Centro Euro-Mediterraneo sui Cambiamenti Climatici (CMCC), Bologna, Italy
- ⁵ Istituto Nazionale di Geofisica e Vulcanologia, Bologna, Italy

Trascasa-Castro et al. 2019; Hardiman et al. 2019; Jiménez-Esteve and Domeisen 2019). The actual “linearity” of the ENSO-NAE teleconnection thus remains unresolved, and addressing this issue is the primary objective of this study.

Another key aspect of the ENSO-NAE teleconnection which is nothing but settled is the dynamical mechanism leading to the canonical SLP dipole. In particular, two main pathways are suggested for this teleconnection: via the troposphere and via the stratosphere. Regarding the tropospheric pathway, the poleward-propagating Rossby wave train (see “Appendix 1”) driving the well-established teleconnection in the North Pacific (Trenberth et al. 1998), first described by Horel and Wallace (1981) and Hoskins and Karoly (1981), is a suitable candidate (e.g. García-Serrano et al. 2011; Mezzina et al. 2020), although other mechanisms have been proposed (e.g. Toniazzo and Scaife 2006; Jiménez-Esteve and Domeisen 2018). The stratospheric pathway would involve a response to ENSO in the extra-tropical stratosphere, typically consisting of changes in the strength of the polar vortex, followed by downward propagation of the anomalies into the troposphere that then trigger North Atlantic Oscillation (NAO)-like variability (see Domeisen et al. 2019 for a review). The two hypotheses are not mutually exclusive, and some studies suggest that El Niño and La Niña may have different preferred pathways, in particular when strong versus weak events are considered (e.g. Hardiman et al. 2019; Trascasa-Castro et al. 2019). The polar vortex response will be briefly examined in this study, which instead focuses on the tropospheric pathway. One of our objectives is to show that the canonical NAE signal associated with El Niño and La Niña can be mostly explained in terms of the same tropospheric dynamics.

The underlying idea of this study is to use idealized experiments with atmospheric models forced by *symmetric* anomalous SST patterns representing El Niño and La Niña to diagnose symmetries and asymmetries in the extra-tropical response. With this approach, potential asymmetries can be attributed purely to atmospheric processes and isolated from other effects related to the ENSO diversity (Capotondi et al. 2015). Previous studies adopted a similar method (e.g. Hoerling et al. 2001), including very recent ones (e.g. Jiménez-Esteve and Domeisen 2019; Trascasa-Castro et al. 2019), but, to the best of our knowledge, it is the first time that this is done in a multi-model framework. The experiments analyzed here are in fact run with the same protocol using three state-of-the-art models; that these models provide consistent results will add robustness to our conclusions. We aim not only at diagnosing asymmetries in the extra-tropical ENSO-related SLP signal, but also at understanding their cause by examining all the steps involved in the tropospheric pathway of the atmospheric response, starting from the tropical Pacific. The interaction of heat-induced anomalies in the tropical upper troposphere with the mean

flow in the sub-tropics is key to understanding SST-forced teleconnections (Sardeshmukh and Hoskins 1988; Qin and Robinson 1993), and it will be carefully examined here in order to trace back the asymmetric behavior of the extra-tropical SLP response.

While we will present results for the entire Northern Hemisphere, including the North Pacific, our primary target is the NAE sector. For this reason, the study is based on late winter (JFM), when the canonical signal is more robust (Brönnimann 2007), since intra-seasonal changes between early winter (November–December) and late winter (January–February) occur (e.g. Moron and Gouirand 2003; Gouirand et al. 2007; Bladé et al. 2008; King et al. 2018; Ayarzagüena et al. 2018). Note that the use of different seasons across NAE-oriented studies may be contributing to the lack of agreement on the symmetric character of the teleconnection.

We will call *asymmetry* any deviation from what is expected to be a linear, symmetric behavior, i.e. an identical pattern with same amplitude but opposite sign for El Niño and La Niña. The term “non-linearity” is often used to describe these deviations but, in the context of the ENSO teleconnection, it may refer to several aspects: the impacts of El Niño versus La Niña (e.g. Hoerling et al. 1997), of strong versus moderate/weak events (e.g. Toniazzo and Scaife 2006), of different ENSO “flavors”, such as the Central Pacific and Eastern Pacific El Niños (e.g. Capotondi et al. 2015). Garfinkel et al. (2019), for example, discuss all these aspects referring to them as “non-linearities”. The last two issues—distinct flavors and strength—are intentionally left out in this work, which focuses on the response to strong, Eastern Pacific-like events of opposite polarity. In this context, the term “non-linearity” could be used without ambiguity, but we choose the more neutral “asymmetry” as it does not suggest the involvement of non-linear physical processes such as the triggering of different pathways.

Another point that will be addressed here, not concerning the asymmetries but of crucial importance for the full understanding of the canonical NAE dipole, is the relationship between the ENSO-forced variability in the Euro-Atlantic sector and the NAO. While Brönnimann (2007) already stressed that the canonical dipole resembles “*though not exactly*” the North Atlantic Oscillation, in the following years little effort was dedicated to distinguishing the canonical “NAO-like” dipole from the NAO itself (e.g. García-Serrano et al. 2011). Here, we adopt a complementary approach to confirm the results of Mezzina et al. (2020), who used reanalysis data and AMIP-like simulations to show that the ENSO-NAE teleconnection, despite some similarity at the surface, is dynamically distinct from the NAO.

After describing the models, experimental protocol and methods in Sect. 2, we examine the tropical and extra-tropical tropospheric response to El Niño- and La Niña-like

forcings across the three models (Sect. 3), and in Sect. 3.5 we compare it to the internal variability associated with the NAO. In Sect. 3.6, we discuss the stratospheric response to EN and LN, and also compare it with the NAO-related variability. We summarize and discuss our results in Sect. 4, while the main conclusions are provided in Sect. 5.

2 Data and Methods

2.1 Models and experimental set-up

All experiments analysed here are atmosphere-only simulations. The multi-model ensemble, contributing to the ERA4CS-funded MEDSCOPE project, consists of three state-of-the-art models. The first one is the atmospheric component of the climate model EC-EARTH3.2, the ECMWF Integrated Forecasting System (IFS) cycle 36r4, at T255 horizontal resolution (approx. 0.7° in longitude-latitude, ~ 80 km) with 91 vertical levels up to 0.01 hPa (see Davini et al. 2017 and Haarsma et al. 2020; hereafter *EC-EARTH*). The second one is the atmospheric component of the climate model CNRM-CM6-1, ARPEGE-Climat v6.3 at T127 horizontal resolution ($\sim 1.4^\circ$ at the equator), also with 91 vertical levels up to 0.01 hPa (see Voldoire et al. 2019; Roehrig et al. 2020; hereafter *CNRM*). Lastly, the atmospheric component of the climate model CMCC-SPS3, CAM5.3, with a horizontal resolution of about 110 km and 46 vertical levels up to 0.3 hPa (see Sanna et al. 2017; hereafter *CMCC*).

The suite of experiments includes a control simulation and two perturbed runs. Observational SSTs (HadISST2.2; Titchner and Rayner 2014) are used to define the boundary conditions, and all radiative forcings are kept fixed at year 2,000 to represent present-day conditions and avoid the effect of long-term trends. The control simulation (CTL) is run with climatological SSTs computed over the period 1981–2010 and integrated for 50 years after spin-up. CTL is also used to provide atmospheric initial conditions for the sensitivity experiments. The latter are designed to study the forced response to symmetric warm and cold ENSO events. The El Niño experiment (EN) is performed with SST anomalies that mimic a strong, canonical eastern-Pacific El Niño event; the La Niña experiment (LN) has identical prescribed pattern but with flipped-sign SST anomalies, i.e. multiplied

by -1 . The time-evolving anomalous SSTs, superimposed on the climatological condition of CTL, are built using linear regressions of detrended monthly SST anomalies onto the Niño3.4 index (area-averaged SST anomalies over 5°N – 5°S ; 170°W – 120°W) in DJF, and over the period 1981–2010 to ensure reliability and quality of data for the ENSO pattern in the satellite era. The EN/LN experiments are run for a complete ENSO cycle, from June 1st (year 0) to May 31st (year 1). The imposed SST anomalies are restricted to 20°S – 20°N (see Fig. 1) and are augmented to reach a maximum amplitude of about 2.7°C (2.4°C) in DJF (JFM), similar to previous studies (e.g. Taguchi and Hartmann 2006), in order to compensate for the damping by surface heat fluxes that results from considering the ocean as an infinite reservoir of heat capacity (atmosphere-only simulations). The amplitude of the SST anomalies is realistic and comparable to the strongest observed El Niño events (1982/83, 1997/98, 2015/16).

2.2 Methods

The forced atmospheric response associated with El Niño (La Niña) is estimated by computing the difference between the ensemble mean of the 50 winters in EN (LN) and CTL; unless otherwise indicated (e.g. Sect. 3.5), we will refer to this response to EN/LN as *forced patterns* or *anomalies*. Several direct outputs of atmospheric fields are examined: sea-level pressure (SLP), 3D geopotential height (Z), and precipitation (PCP). Additionally, to assess the generation of anomalous vorticity that triggers the Rossby wave energy propagation (Sect. 3.3), we compute the Tropical Rossby Wave Source as:

$$TRWS = -v'_\chi \cdot \nabla \left(\bar{\zeta} + f \right)$$

where v'_χ is the anomalous divergent wind, $\bar{\zeta}$ is the climatological relative vorticity, and f is the planetary vorticity or Coriolis parameter (Sardeshmukh and Hoskins 1988; Qin and Robinson 1993); monthly zonal and meridional wind are used to first integrate the velocity potential χ from the divergence, and then to derive the divergent wind v_χ (e.g. Sardeshmukh and Hoskins 1987).

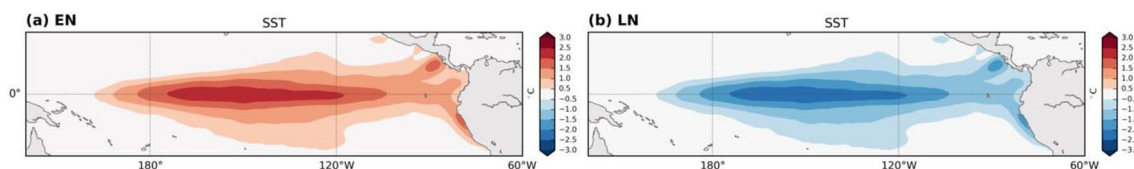
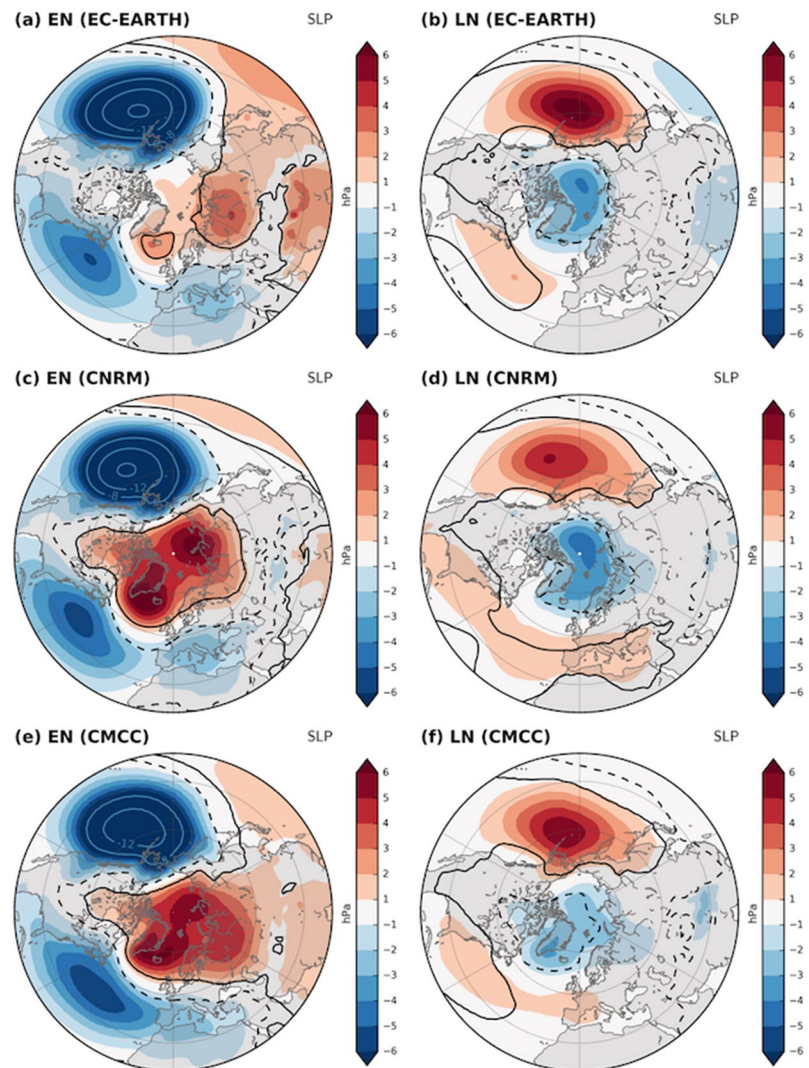


Fig. 1 JFM average of the SST anomalies prescribed in the **a** EN and **b** LN experiments

Fig. 2 Ensemble-mean SLP anomalies for (left) EN and (right) LN with respect to CTL in JFM: EC-EARTH (top), CNRM (middle), CMCC (bottom). Blue contours show values exceeding the color scale limit at -8 , -12 , -16 hPa. Black contours (solid for positive, dashed for negative anomalies) indicate statistically significant areas at the 95% confidence level



In Sect. 3.5 we evaluate changes in storm-track activity by computing the Eddy Kinetic Energy at 500 hPa as (Hoskins et al. 1983; Trenberth 1986):

$$EKE = \frac{1}{2}(u'u' + v'v')$$

where the covariances are computed from daily horizontal wind and applying the 24-h difference filter (e.g. Wallace et al. 1988; Chang et al. 2002) and then performing seasonal averages. Note that other diagnostics such as geopotential height variance at 500 hPa (Blackmon 1976; Lau 1988) or EKE at 200 hPa yield identical results.

CTL is used to study the unforced, internally-generated variability associated with the NAO (Sect. 3.5). Specifically, after defining the NAO index as the 1st Principal Component/EOF of SLP anomalies over the NAE region (20°N – 90°N – 90°W – 40°E), its positive (NAO^+) and

negative (NAO^-) phases are computed based on the upper and lower terciles of the index, respectively, from the 50 winters. Composite NAO^- – NAO^+ maps of different variables, thus displaying patterns with NAO^- polarity, are discussed in Sects. 3.5 and 3.6.

The zonal shift and amplitude ratio between the responses in EN and LN are quantified by first computing, separately in the two experiments, the coordinates of the strongest response in the examined region (x_{max}, y_{max}). For the shift, the difference between the longitudes ($x_{max}^{EN} - x_{max}^{LN}$) is evaluated, with positive values indicating an eastward shift in EN with respect to LN. For the ratio, the area-average over a box centered at (x_{max}, y_{max}) is used to estimate the amplitude of the response in EN and LN, and the ratio between them is computed (EN/LN). The box has varying size according to the variable: $x_{max} \pm 10^{\circ}$ and $y_{max} \pm 5^{\circ}$ for SLP and Z200; $\pm 5^{\circ}$ in both directions for PCP; $x_{max} \pm 5^{\circ}$ and $y_{max} \pm 2^{\circ}$ for TRWS.

As stated in the Introduction, the target of the study is the late-winter ENSO teleconnection and hence all figures are presented for JFM. Statistical significance of the ENSO-forced response and NAO-related internal variability is assessed by applying a Student's *t*-test for the difference of means at the 95% confidence level. An *F*-test for the difference of variances is used in the case of the amplitude ratio, also at the 95% confidence level.

3 Results

3.1 Forced extra-tropical response: sea-level pressure

Looking for insights on the canonical ENSO-NAE teleconnection, we begin by examining the forced SLP patterns in the EN and LN experiments. All models agree in showing the strongest response over the North Pacific: the expected, well-documented deepening of the Aleutian Low in EN (Fig. 2a, c, e) and weakening in LN (Fig. 2b, d, f; e.g. Trenberth et al. 1998; Alexander et al. 2002). Two aspects stand out, given that these patterns are forced by symmetric SST anomalies: (i) the response in LN is much weaker, about half the amplitude of that in EN, and (ii) it is shifted westward with respect to that in EN by about 10°–20°, depending on the model. These features, which will also emerge in other regions and fields, are robust across the three models, and the differences between the forced patterns, namely the asymmetric component of the response (EN + LN), are mostly statistically significant (see Online Resource 1).

In the NAE sector, a dipole with centers of action in mid and high latitudes is present in both EN and LN, with opposite polarity, consistent with the canonical late-winter signature of ENSO (see Introduction). As in the North Pacific, a clear disproportion exists in terms of amplitude between EN and LN, while a westward longitudinal shift of about 20° is also present but not readily apparent due to the less defined nature of the anomalies in LN, probably linked to their weakness (see Sect. 3.4). Some inter-model variability is noticeable: the mid-latitude anomaly varies in shape and extent in LN, and in EN a distinct secondary center of action over the Mediterranean appears in EC-EARTH and CNRM, but not so clearly in CMCC. However, the fundamental structure of the El Niño and La Niña related patterns—i.e. the dipole over the North Atlantic—is consistent among the models.

The surface response to the symmetric ENSO forcing in the Northern Hemisphere thus appears to be roughly symmetric except for the two aspects mentioned above: the zonal shift and the amplitude difference.

3.2 Forced tropical response: convection

What is the origin of the zonal shift and amplitude difference of the extra-tropical ENSO teleconnection? To address this question, we take a step back and examine the deep convection response to the SST forcing in the tropical Pacific. While the prescribed anomalies are symmetric in the two sensitivity experiments (see Sect. 2), the total SST resulting from their combination with the climatology is obviously different; but the full SST field, and the total amount of heating provided, is what ultimately determines the development of tropical convection. First, a threshold of around 27°C is required to trigger deep convection, both in observations (e.g. Graham and Barnett 1987) and models (e.g. Numaguti and Hayashi 1991), a condition that is fulfilled all over the tropical Pacific in EN (yellow contour in Fig. 3a, c, e) but only in the western part of the basin, over the Warm Pool, in LN (Fig. 3b, d, f). Second, tropical convection is related to low-level moisture convergence which is, in turn, affected by the SST gradient (e.g. Lindzen and Nigam 1987; Back and Bretherton 2009). Using total (not anomalous) precipitation as a proxy, we can confirm that the longitude of maximum convection is approximately located where the zonal gradient of SST changes sign (cf. shading and red/blue contours in Fig. 3). Thus, in EN the maximum precipitation north of the Equator is located east of the Date Line (around 170°W; Fig. 3a, c, e), in contrast to LN, which always shows a maximum west of it (around 160°E; Fig. 3b, d, f). In terms of anomalies with respect to CTL, convection/PCP is essentially weakened in LN, while it is enhanced but also shifted to the east in EN (not shown). Therefore, there is a westward shift of tropical convection in LN with respect to EN, consistent with what we noticed in the extra-tropical SLP patterns (Sect. 3.1). The longitudinal shift of the deep convection response, however, varies from 30° to 40°, depending on the model, almost twice the value of the SLP shift in the extra-tropics. The EN/LN amplitude asymmetry observed in the extra-tropical SLP is already apparent in the tropical response, since the precipitation amplitude in LN is about half that in EN, with the exception of CMCC, where they have comparable magnitudes (Fig. 3). Not surprisingly, the overall cooler tropical Pacific in LN provides less diabatic heating and promotes weaker convection with respect to EN, despite the symmetric anomalous SST forcing.

3.3 Forced tropical response: upper-level divergent wind and tropical Rossby wave source

The low-level convergence and associated rising motion are balanced at upper levels by divergent flow; hence, our next step is to examine the anomalous divergent wind (v'_χ) at 200 hPa, which is the level of approximate maximum outflow. In EN, the tropical Pacific is dominated by anomalous

equatorial divergence around 160°E–160°W, consistent with the reinforced convective activity there (cf. Fig. 3a, c, e and Fig. 4a, c, e); convergence is observed to the east and west, at around 100°E and 50°W, resulting from large-scale compensation (e.g. García-Serrano et al. 2017). In contrast, the suppression of climatological convection in LN is manifested as anomalous convergence over the western Pacific (Fig. 4b, d, f). There are, again, no striking differences among the models, except for the overall weaker signal in CMCC (in both EN and LN), in agreement with the response in precipitation.

Anomalous upper-level divergence is the essential trigger of the quasi-stationary large-scale Rossby wave train that constitutes the main extra-tropical response to ENSO (e.g. Trenberth et al. 1998); however, this is only part of the story. The generation of Rossby waves due to tropical heating can be described in terms of the Rossby Wave Source (RWS), a diagnostic that involves the interaction between divergence and vorticity (Sardeshmukh and Hoskins 1988). In particular, the most effective source to excite extra-tropical teleconnections is the advection of climatological vorticity by the anomalous divergent flow (Qin and Robinson 1993), called the tropical component of the Rossby Wave Source (TRWS; see Sect. 2.2). The TRWS is depicted in Fig. 4 (shading); for clarity, some anomalies are masked out in this figure, but the full TRWS is shown and discussed in “Appendix 2” (Fig. 12). The anomalies, with opposite sign, have roughly the same structure in EN and LN: a horseshoe-like pattern with maxima around 5°N and 30°N (the horseshoe shape in LN is not evident due the contour interval, see Fig. 12). These maxima can be explained by examining the two

components of TRWS separately, v'_x and $\nabla(\bar{\zeta} + f)$, shown in Fig. 13 of “Appendix 2”. The gradient of climatological vorticity (computed from CTL) is small in the central tropical Pacific, close to the Equator, but this is where the strongest anomalous divergent wind is found. In contrast, the North Pacific jet is responsible for the strong gradient of climatological vorticity around 30°N that, combined with the moderate v'_x anomalies there, generates the subtropical maximum in TRWS (cf. Figs. 4, 13). Note that the realistic zonally-asymmetric mean flow is what determines the “distorted” horseshoe-like shape of TRWS, which would tend to have zonally-aligned maxima otherwise (Qin and Robinson 1993; Ting 1996). Through the anomalous divergent wind, TRWS inherits part of the asymmetry between EN and LN observed in tropical convection. Using the TRWS maximum located at about 30°N as a reference, the TRWS anomalies in EN are 1 to 2.5 stronger than in LN—depending on the model—, similarly to the difference in precipitation. The zonal shift in convection and in the tropical divergent outflow, on the other hand, is mitigated by the interaction with the mean flow, whereby it decreases from 30° to 40° in precipitation to 20°–30° in TRWS (Fig. 4).

In line with the deep convection response, CMCC is showing a weaker signal compared to the other models in divergent wind and in the TRWS maximum around 5°N, in both EN and LN. The subtropical TRWS maximum, on the other hand, has similar amplitude in all the models. In addition, while in EC-EARTH and CMCC the TRWS anomaly linked to the jet is clearly stronger than the one in the tropics,

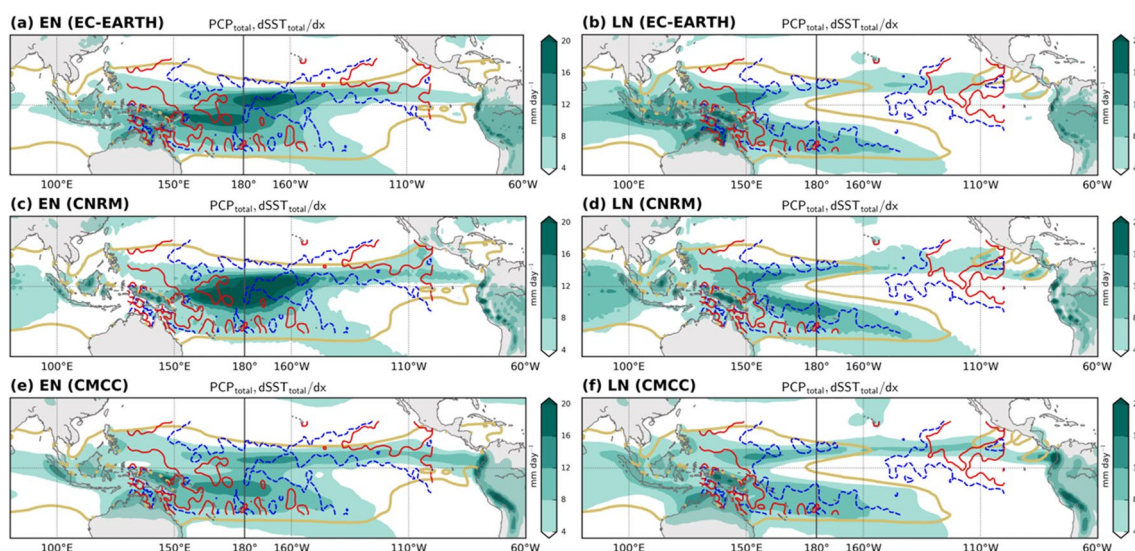


Fig. 3 Ensemble-mean PCP (shading), zonal SST gradient (red and blue contours, indicating $+0.2$ and $-0.2 \cdot 10^{-6} \text{ °C/m}$, respectively) and SST at 27 °C (yellow contour) for (left) EN and (right) LN in

JFM: EC-EARTH (top), CNRM (middle), CMCC (bottom). For clarity, the zonal SST gradient is smoothed and only shown in the box 130°E–100°W; 20°S–20°N

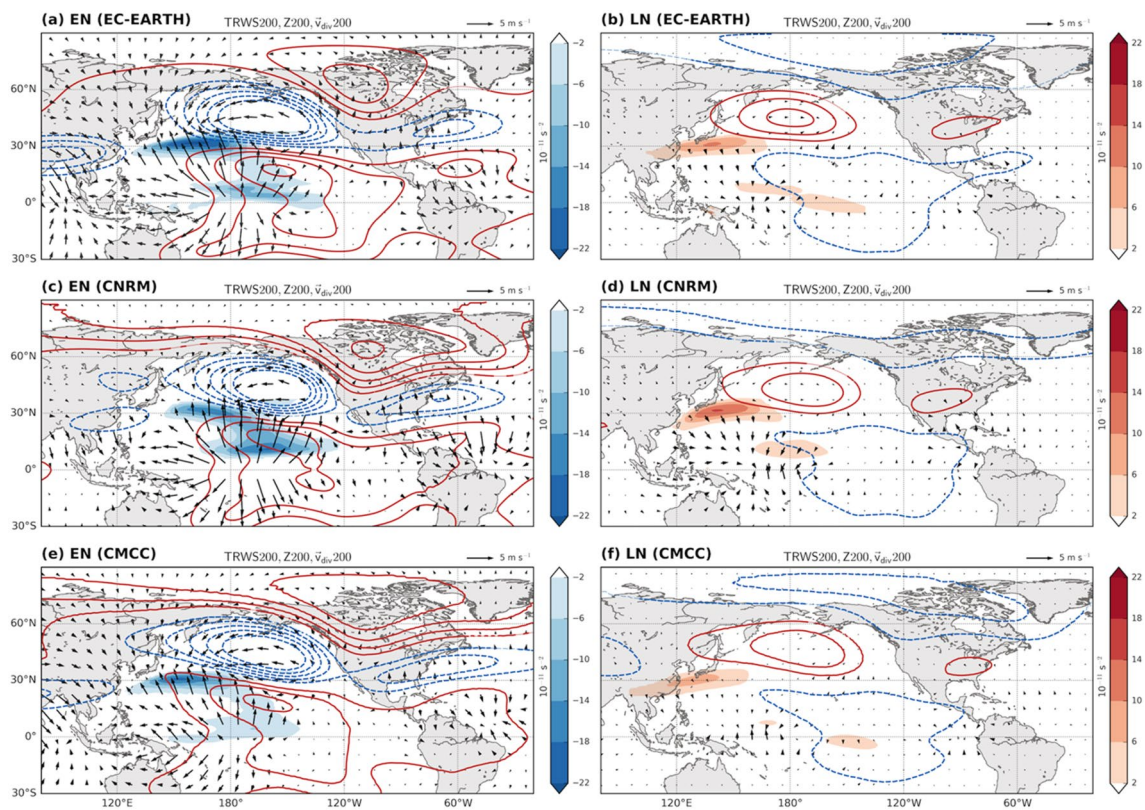


Fig. 4 Ensemble-mean 200-hPa TRWS (shading), divergent wind (arrows) and Z200 (contours; interval=30 m) anomalies for (left) EN and (right) LN in JFM: EC-EARTH (top), CNRM (middle), CMCC (bottom). For TRWS, only the strongest negative (positive) anomalies

in the tropical North Pacific are shown in EN (LN), see Fig. 12 for the full field. Only statistically significant TRWS and $\bar{v}'_{div,200}$ anomalies (95% confidence level) are shown. For Z200, non-significant values are plotted with lighter contours

in CNRM the two appear to have comparable magnitude in EN, probably because of the very intense rainfall response and hence anomalous divergent wind (Fig. 4c).

3.4 ENSO-forced extra-tropical response: upper levels

After examining the Rossby Wave Source, the following step is to finally turn to the forced wave train itself. As it is conventionally detected in the upper-level (200 hPa) geopotential height, its anomalies for the two sensitivity experiments are shown as contours in Fig. 4. A succession of highs and lows curving away from the tropical Pacific is evident in both EN and LN, with opposite signs, forming the well-known arching wave train (e.g. Horel and Wallace 1981; Hoskins and Karoly 1981).

Starting from the ENSO region and focusing on the extra-tropics, poleward of 30°N, the first center of action is found in the North Pacific. In EN, it is centered east of the Date Line and extends up to the western coast of North America, while in LN it is shifted westward by about 10°–20°, roughly straddling the Date Line and reaching the western boundary of the basin. This well-known center of action is the

upper-tropospheric counterpart of the SLP anomalies in the North Pacific (Aleutian Low) described in Sect. 3.1. The high (low) in EN (LN) approximately located over Canada and covering the polar region is the second center of action of the wave train; while in EN it has a clear center and consistent location across the models, it looks less defined in LN, particularly in the cylindrical projection that is used here. Finally, the tail of the wave train reaches the western mid-latitude North Atlantic in EN, but its LN equivalent is located inland over North America. There is some inter-model variability concerning this zonal shift, which ranges from 15° to 35°, but the shift is overall larger than the one in the North Pacific. On the other hand, the EN/LN asymmetry in amplitude is a common aspect to all the anomalies belonging to the wave train: the extra-tropical upper-level response in EN is about double the response in LN.

On a side note, we highlight that the tropical Gill-type response (Matsuno 1966; Gill 1980) does not exhibit a clear shift in longitude, but only weaker amplitude in LN compared to EN, consistent with the weaker signal in tropical convection.

3.5 ENSO-forced extra-tropical response: a closer look at the North Atlantic

The tail of the ENSO-induced wave train projects at the surface on the mid-latitude lobe of the SLP dipole in the North Atlantic discussed in Sect. 3.1. This is clearly revealed by computing height-longitude cross sections of the anomalous geopotential height averaged over the latitudinal band between 35°N–45°N, which is approximately where the Z200 and SLP mid-latitude anomalies are found in the NAE sector (Figs. 2, 4). The vertically tilted structure, depicted in Fig. 5, shows a maximum around 200 hPa that corresponds to the center of action over the western North Atlantic in Z200 (Fig. 4), while the amplitude decreases towards the surface, consistent with the fact that the maximum tropical outflow and thus the maximum TRWS occur at upper levels (Jin and Hoskins 1995; Ambrizzi and Hoskins 1997) and with the structure of balanced stationary waves in an atmosphere in which the zonal wind increases with height (Held et al. 2002). The SLP center over the mid-latitude North Atlantic (Fig. 2) is part of this 3-dimensional anomalous structure. In LN the vertical pattern is less defined, but the eastward shift of the surface response with respect to the upper-level maximum is still evident (Fig. 5b, d, f). In Fig. 5, the westward shift of the whole anomalous pattern in LN with respect to EN is consistent with those described in Sects. 3.1 and 3.4. The maximum at the surface in LN is not as evident as in EN (see also Fig. 2), but, if we follow the general westward tilt with height of the pattern and consider the maximum at upper levels, the longitude of the surface maximum can be estimated to be around 60°W (80°W) in EN (LN), implying a zonal shift of about 20°.

The westward tilt with height is an intrinsic feature of large-scale Rossby waves and it provides important information on the dynamics of the ENSO-related SLP dipole in the NAE sector, particularly in the context of the debate around its relationship with the NAO (see Introduction and Mezzina et al. 2020). To investigate this issue, we examine the NAO-related variability in the three models by considering the CTL experiment, where the variability is purely internal to the atmosphere (see Sect. 2). The distinctive signature of the NAO in SLP, a dipole in the North Atlantic, is accurately reproduced by all models (Fig. 6a, c, e). There is a certain similarity with the ENSO patterns of Fig. 2 (see also Fig. 11 in “Appendix 1”), but note how the NAO-related mid-latitude anomaly is centered around the zero Meridian, almost in quadrature with the ENSO-forced patterns, particularly for EC-EARTH (cf. Figs. 2, 6a). This surface pattern is accompanied by upper-level anomalies (Z200) that are essentially barotropic, with no vertical tilt, over the North Atlantic (Fig. 6b, d, f) and are reminiscent of the circumglobal waveguide pattern on the hemispheric scale (Branstator 2002). Extending the analysis to transient-eddy

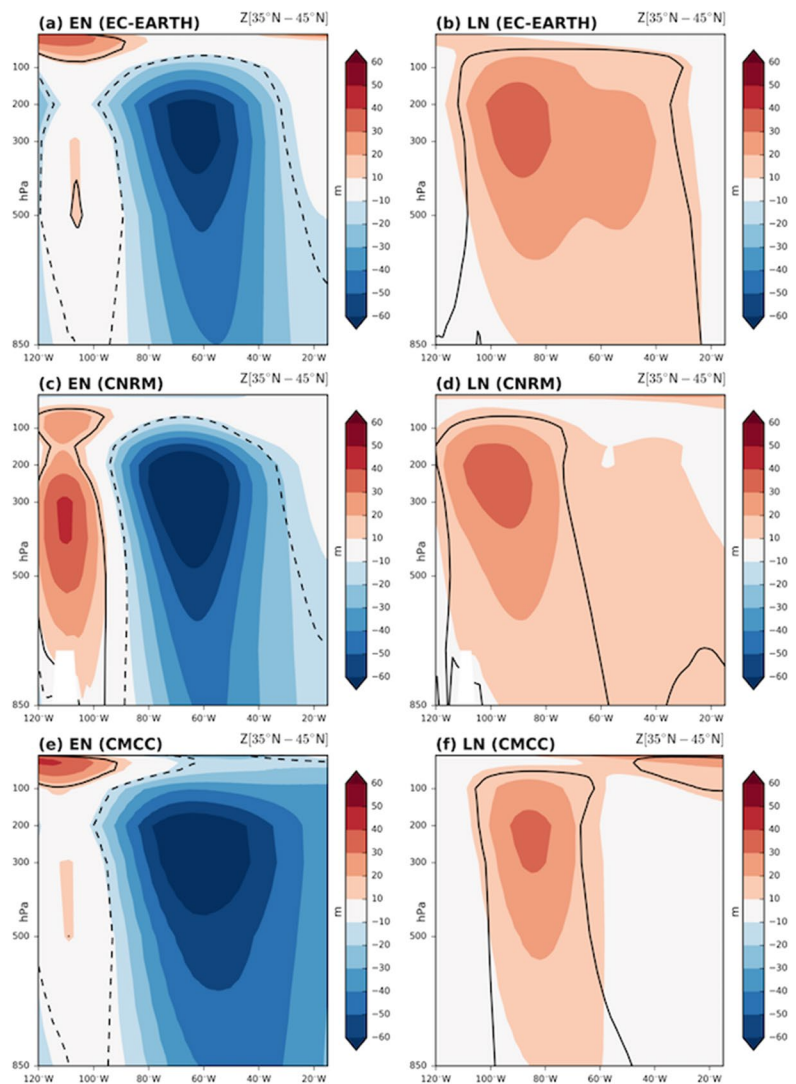
activity, the NAO meridionally shifts the storm tracks reaching western Europe, leading to a wet-dry dipole in precipitation there (Fig. 7c, f, i). In contrast, the impact of ENSO is more limited to the North Atlantic Ocean (left and middle columns of Fig. 7), with its maximum anomaly in EKE located approximately at the node of the NAO signal. This longitudinal distinction between the ENSO-forced and NAO-related patterns is robust across the models and statistically significant (not shown).

3.6 ENSO-forced extra-tropical response: lower stratosphere

Following the numerous studies suggesting that the ENSO-NAE teleconnection may be, partially or totally, driven by the stratospheric pathway (see Introduction), it is worth exploring the models’ response in the lower polar stratosphere (50 hPa geopotential height, Z50; e.g. Ineson and Scaife 2009). In Fig. 8 (left and middle columns), displaying Z50 anomalies, it can be seen that the models show a signal consistent with previous studies (see Brönnimann 2007 for a review): a dominant positive (negative) anomaly in EN (LN) indicating the weakening (strengthening) of the polar vortex, accompanied with weaker, opposite-signed centers of action over the North Pacific and North Atlantic. The signal is roughly symmetric in sign, but the vortex response in EN is stronger than in LN, with the exception of EC-EARTH (Fig. 8a, b) where the positive anomaly in EN is rather weak and confined to central-northern North America, similarly to the corresponding center of action in Z200 (cf. Figs. 4a, 8a). The three models agree in the North Pacific, where the signal is consistent with the tropospheric wave train, displaying a similar longitudinal shift and a slightly weaker magnitude in LN with respect to EN, suggesting a tropospheric origin of the Z50 anomalies.

Less consistency is found in the North Atlantic, where a significant signal in LN is present only in CMCC, roughly symmetric to EN (cf. Fig. 8g, h), although all three models yield the canonical SLP dipole (Fig. 2). But it is actually in the NAE sector where the stratosphere is suggested to play an important role, a hypothesis mainly inspired by the tendency of stratospheric vortex anomalies to project onto dipolar, NAO-like patterns on seasonal time scales (e.g. Hitchcock and Simpson 2014; see Kidston et al. 2015 for a review). For this reason, similarly to the previous section, we also examine the NAO-related variability in CTL. The strongest center of action is still in the polar vortex (Fig. 8c, f, i), but the shape of the circulation anomalies is different than the ENSO-forced response: the configuration of the anomalous vortex in the NAO pattern covers the whole polar cap but is elongated along the axis western North Atlantic-eastern Eurasia (Fig. 8c, f, i), while in EN and LN the vortex anomalies are confined to the western hemisphere (left

Fig. 5 Longitude-height cross section of ensemble-mean geopotential height anomalies for (left) EN and (right) LN with respect to CTL in JFM, averaged over the latitudinal band 35°N–45°N: EC-EARTH (top), CNRM (middle), CMCC (bottom). Black contours (solid for positive, dashed for negative anomalies) indicate statistically significant areas at the 95% confidence level



and middle columns of Fig. 8), except for EN in CNRM (Fig. 8d). These differences can be emphasized with a wavenumber decomposition of the patterns, which shows that the wavenumber-1 component of EN and LN is almost in quadrature with the NAO-related component (Fig. 9). A similar orthogonality of the patterns is also found in the wavenumber-2 component (see “Appendix 3”).

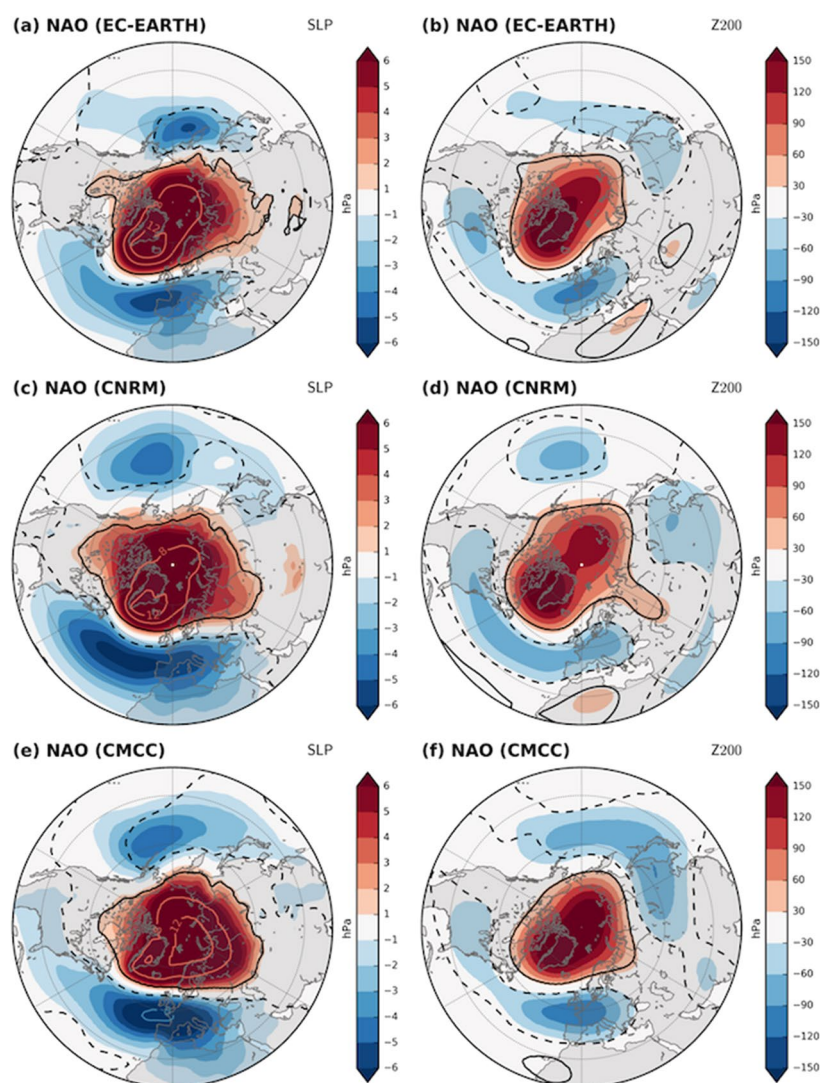
4 Summary and discussion

To guide the discussion, we summarize our results in a schematic figure (Fig. 10). For each model and variable examined (PCP, SLP, TRWS, SLP, Z200), we build a scatter plot of the longitudinal shift in LN relative to EN versus the ratio of the amplitudes, computed as described in Sect. 2.2. For clarity, we consider the North Pacific (Fig. 10a) and the

North Atlantic (Fig. 10b) separately and focus on the mid-latitude response. The two panels thus show the same points for TRWS and PCP, which represent the response over the tropical Pacific, but different ones for SLP and Z200, which describe the mid-latitude signal in the two regions. Note that we used the subtropical maxima of TRWS (at 30°N) to encapsulate the behavior of the TRWS anomalies, as this maximum is more clearly defined than the one in the equatorial region. The purpose of this figure is not to find a relationship between the shift and ratio, but to summarize how the fields behave in response to the symmetric forcing mimicking El Niño and La Niña.

The left panel describes the asymmetric behavior in the North Pacific (blue symbols), in terms of both amplitude, with EN showing anomalies 2–3 times larger than LN, and location, with a shift of 10°–20° (Fig. 10a). This result, which applies to strong El Niño- and La Niña-like SST

Fig. 6 SLP (left) and Z200 (right) composites of NAO⁻–NAO⁺ for CTL in JFM: EC-EARTH (top), CNRM (middle), CMCC (bottom). Red and blue contours show values exceeding the color scale limit at ± 8 , ± 12 , ± 16 hPa. Black contours (solid for positive, dashed for negative anomalies) indicate statistically significant areas at the 95% confidence level



forcings, is in agreement with previous works using similar sensitivity experiments (e.g. Hoerling et al. 1997, 2001; Sardeshmukh et al. 2000; Jiménez-Estève and Domeisen 2019; Tracasa-Castro et al. 2019) but is in conflict with Rao and Ren (2016b), who reported no asymmetry for strong events. In the same study, however, Rao and Ren observed asymmetries in coupled experiments for both the strong and moderate case. On the other hand, the composites in Garfinkel et al. (2019), who used AMIP-like experiments, also show a longitudinal shift and amplitude difference between El Niño and La Niña (see their Fig. 1), although the authors do not comment on them. Observational studies using reanalysis data deliver mixed conclusions as well. De Weaver and Nigam (2002) found a symmetric upper-level response with only a small longitudinal shift ($\sim 10^\circ$), while Deser et al. (2017) report no significant nonlinearities in SLP and only indicate regional differences in amplitude, although their

results show a zonal shift consistent with the one found here (see their Fig. 10). Composites using ECMWF ERA-20CR in JFM lead to a similar result, with minor—but significant—differences in the North Pacific (see “Appendix 4”). In contrast, Hoerling et al. (1997, 2001) and Rao and Ren (2016a) point out clear asymmetries. With some limitations, discussed below, our study advocates for an asymmetric response to El Niño and La Niña in sea-level pressure, which is directly inherited from the upper tropospheric Rossby wave train (cf. SLP and Z200 in Fig. 10a). Convection in the tropical Pacific appears to be the primary source of this asymmetry, but with an even larger shift (Fig. 10a, green). Once the interaction between the anomalous tropical divergence and the climatological vorticity is considered via the TRWS (Fig. 10a, red), the shift is reduced and approaches that in SLP and Z200, with the three variables tending to cluster in the scatter plot.

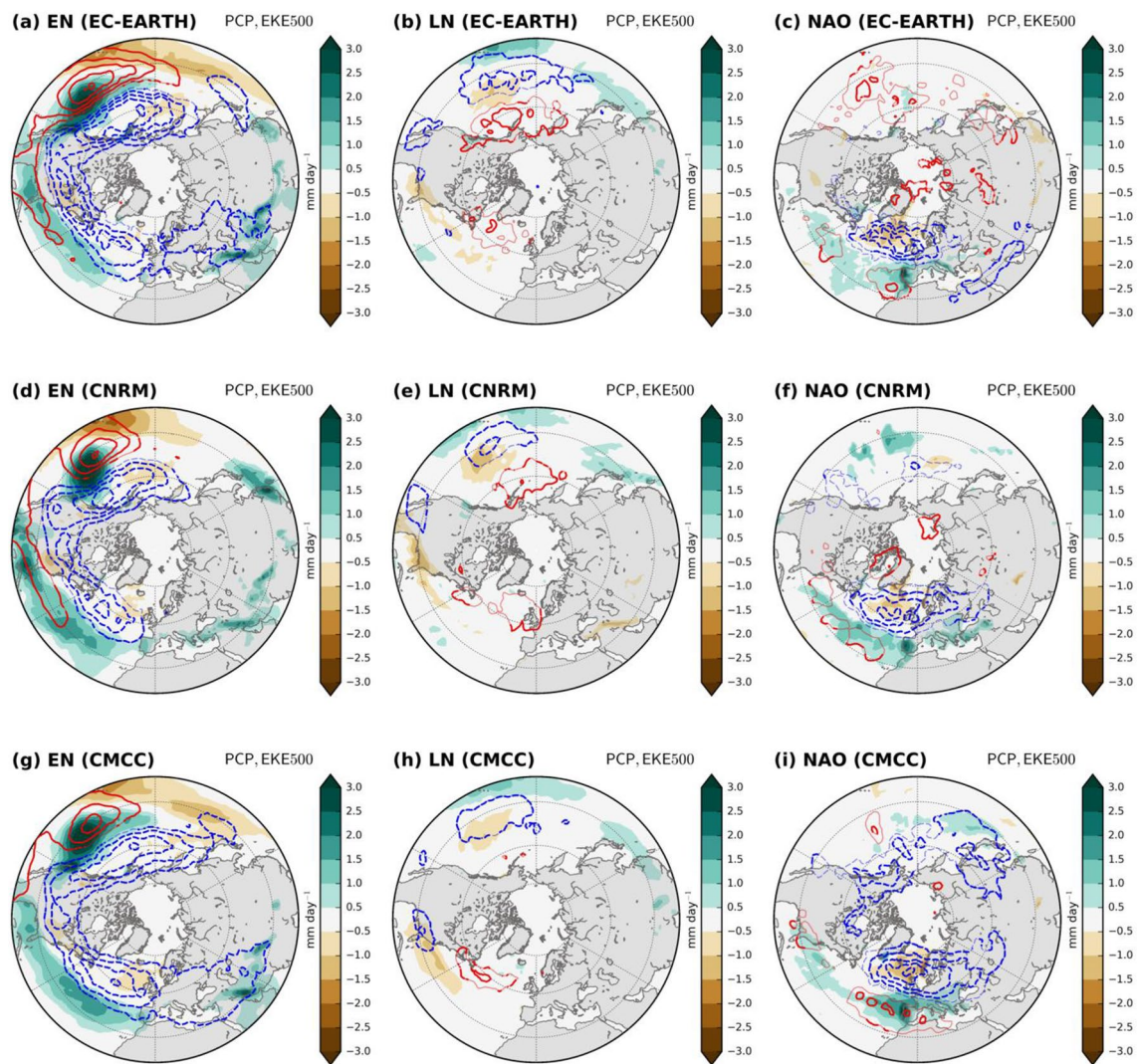


Fig. 7 Left and middle columns: ensemble-mean PCP (shading) and 500-hPa EKE (contours; interval = $8 \text{ m}^2 \text{ s}^{-2}$) anomalies for EN (left) and LN (right) with respect to CTL in JFM: EC-EARTH (top), CNRM (middle), CMCC (bottom). Right column: same, but for

NAO⁻–NAO⁺ in CTL. Only statistically significant PCP anomalies (95% confidence level) are shown. For EKE, non-significant values are plotted with lighter contours

While some consistent asymmetries are still present, the overall picture in the North Atlantic is not as clear as in the North Pacific (Fig. 10b). Z200 has a ratio comparable to the North Pacific, around 2, but larger values and spread for the shift, which ranges from 15° to 35° . For two of the models, the shift is closer to that of TRWS than to that in precipitation (not so in CNRM), confirming the importance of the interplay between the anomalous tropical divergence and the mean flow. The large deviation of SLP from the rest of the variables in the scatter plot is linked to the ratio rather than the shift, partly because the upper-level Rossby wave train in LN projects onto land at the surface, tending to vanish (Fig. 5; e.g. Branstator 2002) and partly because of the large internal atmospheric variability in the region (e.g. Deser et al. 2017). Most observational studies indicate

a large degree of linearity of the ENSO-NAE teleconnection in late-winter, such as Ayarzagüena et al. (2018), although an amplitude asymmetry is present in their composites, and Brönnimann (2007). Focusing on DJF, Deser et al. (2017) found minor, non-significant asymmetries consistent with those in Fig. 15 for JFM, while the monthly maps of Jiménez-Esteve and Domeisen (2018) display a complex, non-linear response from December to March. For Zhang et al. (2019), who separate Central Pacific and Eastern Pacific events, there is no linearity at all for the latter (in JFM). Works using simulations and specifically addressing asymmetries in the North Atlantic are relatively limited in number. Earlier studies include Sardeshmukh et al. (2000) and Pozo-Vazquez et al. (2001), who reported asymmetries in the region, and recently a renewed interest in this topic has

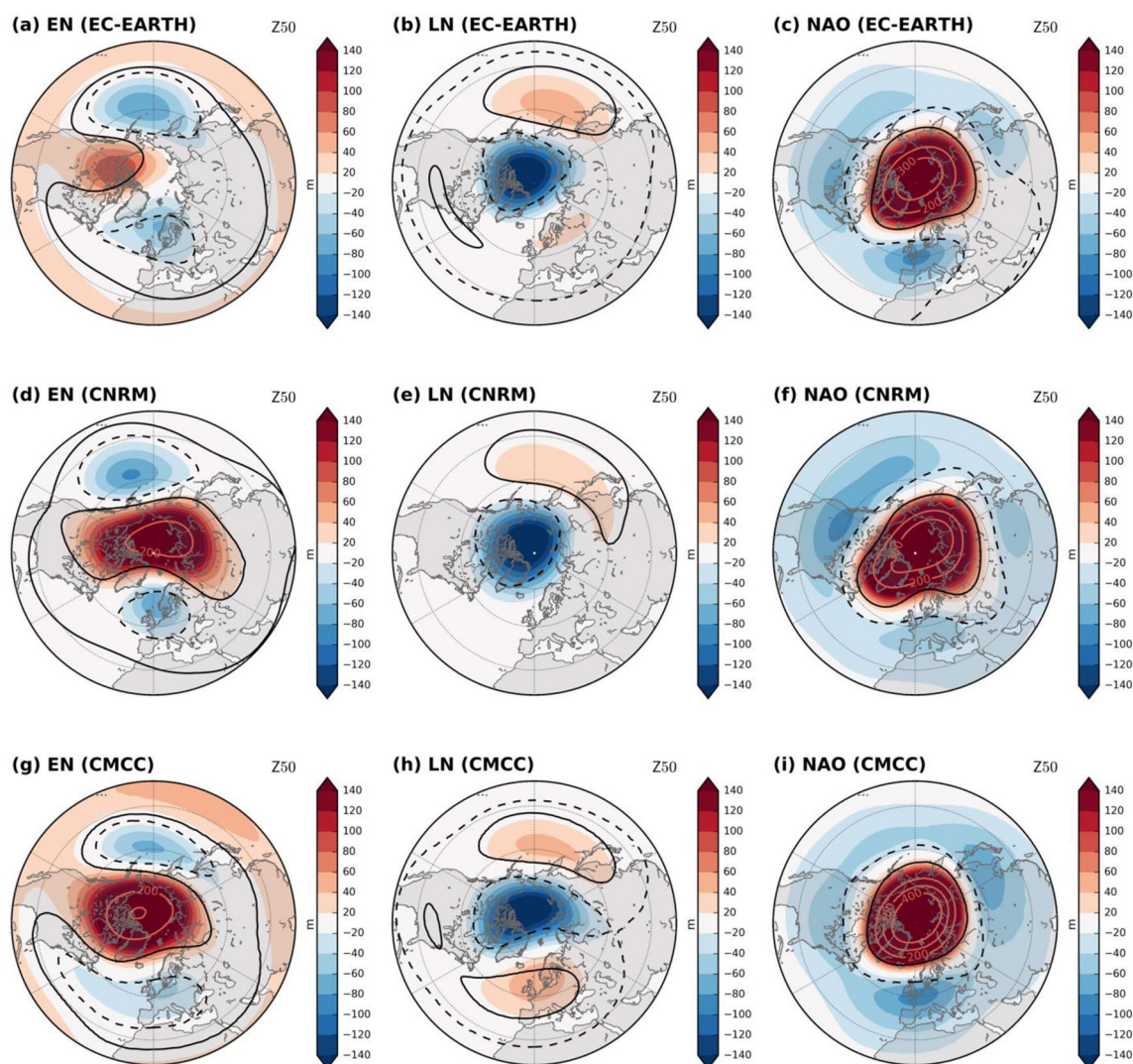


Fig. 8 Left and middle columns: ensemble-mean Z50 anomalies for EN (left) and LN (right) with respect to CTL in JFM: EC-EARTH (top), CNRM (middle), CMCC (bottom). Right column: same, but for NAO⁻–NAO⁺ in CTL. Red and blue contours show values exceeding

the color scale limit at ± 200 , ± 300 , ± 400 m. Black contours (solid for positive, dashed for negative anomalies) indicate statistically significant areas at the 95% confidence level

arisen. Jiménez-Esteve and Domeisen (2019), using a set-up similar to ours but with an intermediate-complexity model, identified asymmetries in the North Atlantic for strong ENSO events, but did not discuss their origin in depth. Trascasa-Castro et al. (2019), Hardimann et al. (2019) and Weinberger et al. (2019), using sensitivity experiments, coupled models and AMIP-like simulations, respectively, reached contrasting conclusions: asymmetry in the first two cases and symmetry in the latter. A common aspect to these three studies, in spite of the different results, is the analysis and discussion of the role of the polar stratosphere. In particular, Weinberger et al. (2019) report no significant “non-linearity” in the presumed stratospheric pathway to the NAE in winter, but a weaker amplitude in the tropospheric circulation for

La Niña compared to El Niño is present in their composites (see their Fig. 1).

Our results suggest that asymmetries are present in the NAE region associated with strong El Niño- and La Niña-like SST patterns in terms of amplitude and zonal shift, but the structure of the SLP pattern is similar and driven by the same dynamics: the dipolar pattern, consistent with the canonical view of Brönnimann (2007), is associated with the tropospheric Rossby wave train and its westward tilt with height (Fig. 5). In addition, comparison of the ENSO- and NAO-related patterns in SLP, Z200, transient-eddy activity and precipitation in the forced and control experiments indicate dynamical differences between the ENSO-NAE teleconnection and the NAO (Figs. 6, 7), supporting the conclusions

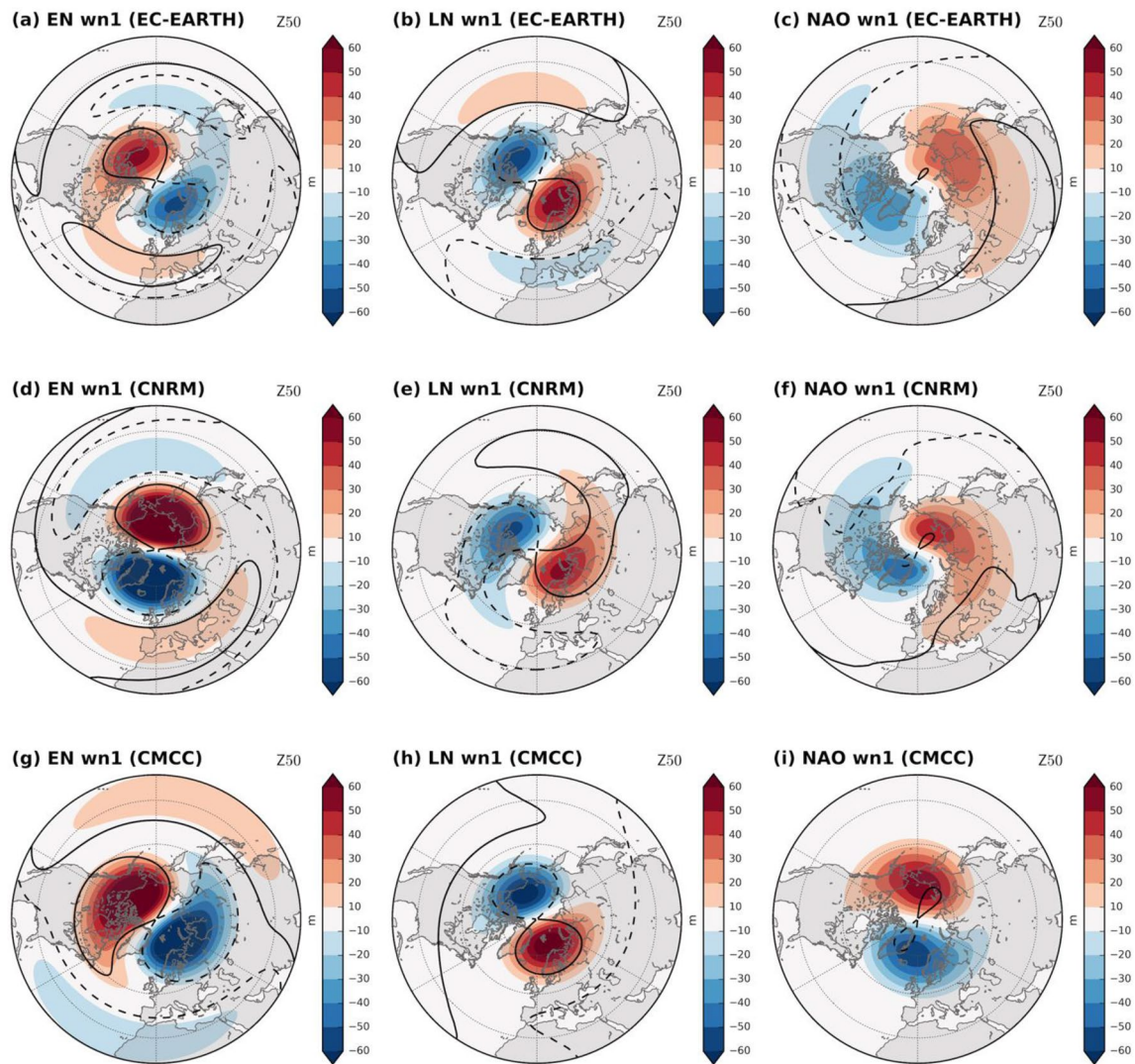


Fig. 9 Left and middle columns: wavenumber-1 component of the ensemble-mean Z50 anomalies for EN (left) and LN (right): EC-EARTH (top), CNRM (middle), CMCC (bottom). Right column:

same, but for NAO⁻–NAO⁺ in CTL. Black contours (solid for positive, dashed for negative anomalies) indicate statistically significant areas at the 95% confidence level

of Mezzina et al. (2020) based on reanalysis and AMIP-like experiments. The stratospheric response to ENSO, which is quite linear in sign but with a consistent asymmetry in amplitude (Fig. 8), does not project onto the NAO-related pattern either; instead, their wavenumber-1 and 2 components are largely orthogonal (Figs. 9, 14).

Note that, when discussing the asymmetries, we do not examine in-depth the other lobe of the NAE dipole—the one at high latitudes—because of its distorted structure at the surface. However, we consider that the two opposite-signed anomalies over the North Atlantic belong to the same dipolar system and are primarily driven by the same tropospheric dynamics, i.e. the Rossby wave train triggered from the tropical Pacific. Therefore, we draw our conclusions indistinctly for the entire dipole of the ENSO-NAE teleconnection.

Some notes on the strength and limitations of the experimental set-up follow. The anomalous SST patterns prescribed as forcing are built from linear regression onto the Niño3.4-index and the same shape, with flipped sign, is used to represent El Niño and La Niña. Several studies adopted the same approach (e.g. Hoerling et al. 2001; Rao and Ren 2016b; Jiménez-Estève and Domeisen 2019; Tracasa-Castro et al. 2019), which here we justify by the aim of focusing on asymmetries arising from one source only, i.e. cooling versus warming of the tropical Pacific, while excluding other factors such as pattern diversity, variations in timing and SST amplitude differences. More importantly, not only are El Niño and La Niña represented with the same spatial pattern, but also with same amplitude, in contrast with the observed skewness: indeed, La Niña events comparable to

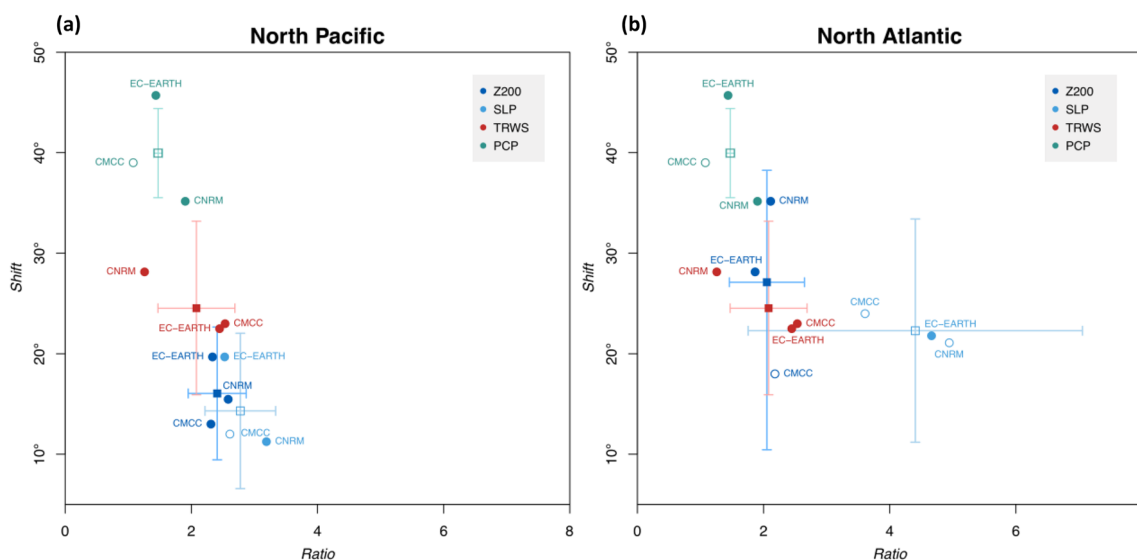


Fig. 10 Shift-ratio scatter plots summarizing the asymmetries in the EN and LN experiments. The maximum response in EN and LN is considered. The horizontal axis indicates the ratio of the amplitudes (EN/LN, positive sign), while the vertical axis represent the longitudinal shift in LN relative to EN. The response over the tropical Pacific is considered for PCP and TRWS, and over the mid-latitude North

Pacific (left) and North Atlantic (right) for SLP and Z200. See text for details. Unlabeled squares represent the multi-model ensemble mean. All points are significant at the 95% confidence level for the shift, while empty circles and squares indicate variables that do not pass the significance test for the ratio. Error bars indicate $\pm 0.5\sigma$ for the multi-model mean

the strongest El Niños are not present in the observational records (e.g. Burgers and Stephenson 1999; Timmermann et al. 2018). Recently, Hardiman et al. (2019) emphasized this lack of “strong” La Niñas in observations and stressed the need to fill this gap with model studies, as such events may happen in the future. “Unrealistically” strong La Niñas are also considered in Jiménez-Esteve and Domeisen (2019) and Tracasa-Castro et al. (2019). As discussed above, these and other similar studies deliver contrasting conclusions concerning the asymmetric response to strong and weak El Niño versus La Niña, particularly in the North Atlantic, stressing the need to further investigate the dynamics of the atmospheric teleconnection of strong ENSO events of both signs. In this context, our study provides relevant contributions to address this gap, with consistent results that are supported by three different state-of-the-art models.

Finally, note that in the analysis of the Rossby Wave Source (Sect. 3.3) we did not include its extra-tropical component, $ERWS = -(\zeta + f)\nabla \cdot v'_{\chi}$, as it is considered to be part of the response and associated with wave propagation (Qin and Robinson 1993; Ting 1996). Works including both terms suggest another source region in the Gulf of Mexico/Caribbean Sea to explain the ENSO-forced SLP dipole in the NAE sector (e.g. Hardiman et al. 2019). This source, which is present in our experiments (see ERWS in Online Resource 2) and also reflected in TRWS (Fig. 12), is related to the large-scale response of the Atlantic Hadley cell to the ENSO-induced changes in convection over northern South America (e.g. Wang 2005; García-Serrano et al. 2017), but

is located downstream of the Rossby wave train crossing the North Pacific (Fig. 4) that is our target. On the other hand, notice that the zonal shift described for TRWS, underlying the longitudinal shift in the ray path of EN/LN, is mirrored in ERWS as both follow the displacement of the Pacific Hadley cell in response to ENSO, the former over the subtropics and the latter in the extra-tropics (north of 30°N).

5 Conclusions

Analyzing sensitivity experiments with symmetric SST forcing mimicking strong warm and cool ENSO events, and using three state-of-the-art models, we draw the following conclusions:

- Even in the presence of a symmetric forcing, asymmetries arise in the SLP response over both the North Pacific (Aleutian Low) and NAE sector (North Atlantic dipole). The response to La Niña SST anomalies tends to be weaker and shifted westward relative to the one associated with El Niño anomalous forcing. This asymmetry is mostly inherited from the large-scale extra-tropical Rossby wave train excited in the upper troposphere.
- The response of tropical convection to the SST forcing is the underlying cause for the extra-tropical asymmetries. Warm (cold) SST anomalies during EN (LN) superimposed onto the mean state enlarge (restrict) the region suitable for the triggering of deep convection (SST above

27 °C) and increase (decrease) the amount of available diabatic heating, while the longitude of maximum convection is found east (west) of the Date Line due to the different SST gradient.

- The anomalous deep convection triggers a similarly shifted anomalous divergent wind response. In order to explain the more modest longitudinal shift of the extra-tropical SLP signal, the anomalous divergence needs to be considered in tandem with the mean flow (Rossby Wave Source).
- The ENSO surface signal in the NAE sector is the “canonical” dipole between mid and high latitudes, with asymmetries in terms of amplitude and longitude but not structure. These asymmetries are not indicative of different mechanisms driving the teleconnection for El Niño and La Niña. Instead, in both cases the ENSO teleconnection to the North Atlantic is mainly associated with the downstream part of the Rossby wave train from the tropical Pacific and its tilt with height, and it is unrelated to the NAO dynamics.

Our results show that ENSO does not trigger NAO-related variability neither in the troposphere nor in the stratosphere, thus questioning the view of the ENSO-NAE teleconnection as an excitation of the NAO via the stratosphere. Hence, we suggest that the dynamics of the stratospheric pathway may need to be revisited.

Finally, we remark on an issue that was mentioned in Sect. 3.4: the tropical signal in Z200, which does not display a clear zonal shift between EN and LN, unlike the extra-tropical one (Fig. 4). The theoretical frameworks describing the tropical Gill-type response and the extra-tropical Rossby wave train are distinct, the former being largely baroclinic and the latter barotropic (e.g. Lee et al. 2009; Ting 1996) and it is not clear whether they are part of the same global-scale response. As remarked by De Weaver and Nigam (2002),

the equatorial response has received little attention and still, 18 years later, a satisfactory description reconciling the tropical and extra-tropical responses is missing.

Acknowledgements This work was supported by the MEDSCOPE project. MEDSCOPE is part of ERA4CS, an ERA-NET initiated by JPI Climate, and funded by AEMET (ES), ANR (FR), BSC (ES), CMCC (IT), CNR (IT), IMR (BE) and Météo-France (FR), with co-funding by the European Union (Grant 690462). B.M. and J.G.-S. were supported by the “Contratos Predoctorales para la Formación de Doctores” (BES-2016-076431) and “Ramón y Cajal” (RYC-2016-21181) programmes, respectively. F.M.P. was partially supported by the Spanish DANAE (CGL2015-68342-R) and GRAVITOCAST (ERC2018-092835) projects. Technical support at BSC (Computational Earth Sciences group) is sincerely acknowledged. We also thank four anonymous reviewers for their valuable insights.

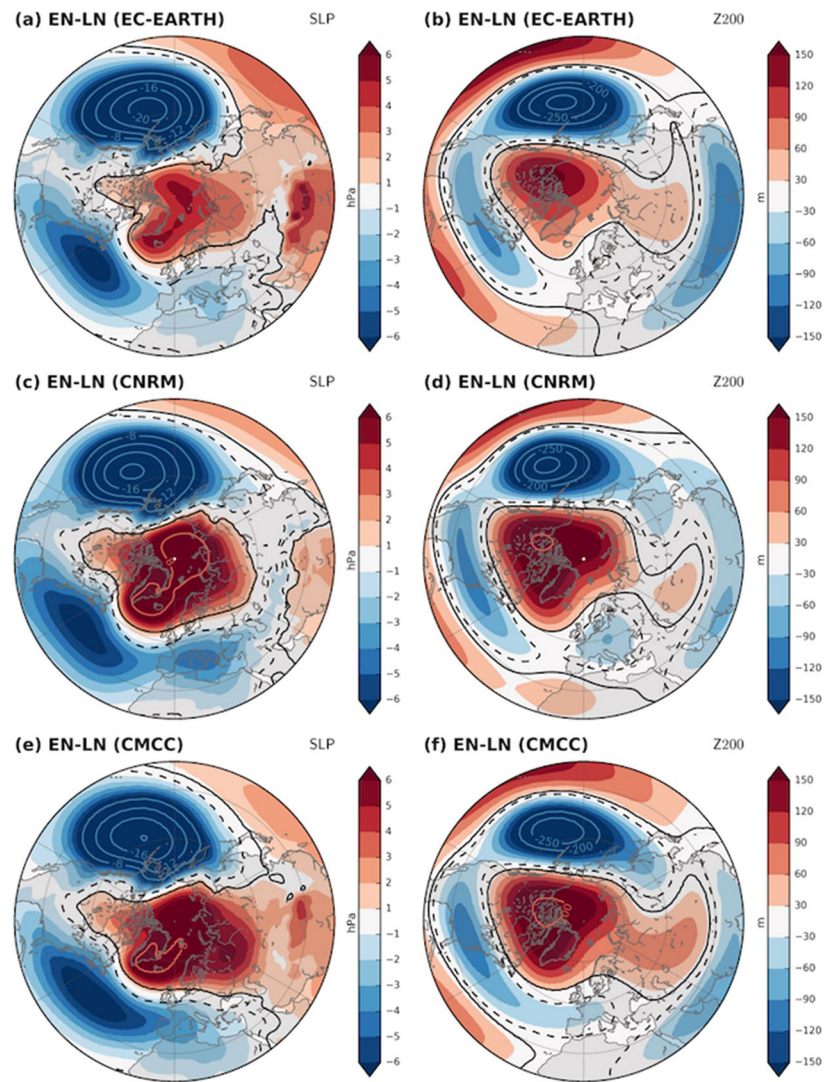
Open Access This article is licensed under a Creative Commons Attribution 4.0 International License, which permits use, sharing, adaptation, distribution and reproduction in any medium or format, as long as you give appropriate credit to the original author(s) and the source, provide a link to the Creative Commons licence, and indicate if changes were made. The images or other third party material in this article are included in the article’s Creative Commons licence, unless indicated otherwise in a credit line to the material. If material is not included in the article’s Creative Commons licence and your intended use is not permitted by statutory regulation or exceeds the permitted use, you will need to obtain permission directly from the copyright holder. To view a copy of this licence, visit <http://creativecommons.org/licenses/by/4.0/>.

Appendix

Appendix 1: Linear response

Figure 11 shows the linear component of the ENSO response in SLP and Z200, i.e. ensemble-mean differences between EN and LN. The benchmarks of the ENSO-NAE teleconnection discussed in the Introduction, the SLP dipole and the large-scale Rossby wave train, are evident in the three models.

Fig. 11 Ensemble-mean SLP (left) and Z200 (right) differences between EN and LN in JFM: EC-EARTH (top), CNRM (middle), CMCC (bottom). Red and blue contours show values exceeding the color scale limit at ± 8 , ± 12 , ± 16 , ± 20 hPa (SLP) and ± 200 , ± 250 , ± 300 m (Z200). Black contours (solid for positive, dashed for negative) indicate statistically significant areas at the 95% confidence level



Appendix 2: Full TRWS and TRWS components

Figure 12 complements Fig. 4 by depicting the full TRWS anomalies (only statistically significant values are shown); the contours are adapted to show the horseshoe-like pattern in LN.

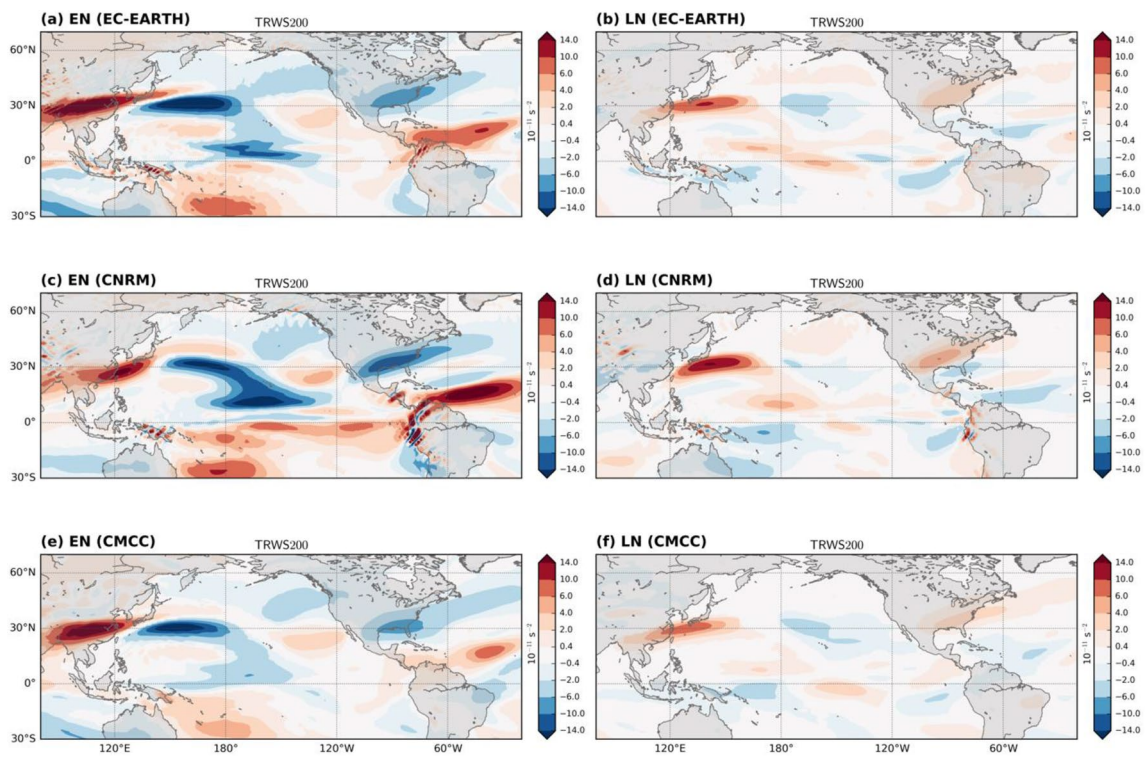


Fig. 12 Ensemble-mean 200-hPa TRWS anomalies for (left) EN and (right) LN with respect to CTL in JFM: EC-EARTH (top), CNRM (middle), CMCC (bottom). Only statistically significant anomalies (95% confidence level) are shown. Anomalies are smoothed in CMCC for clarity

Figure 13 is provided to help the interpretation of the TRWS response by displaying separately its components, v'_x and $\nabla \left(\bar{\zeta} + f \right)$.

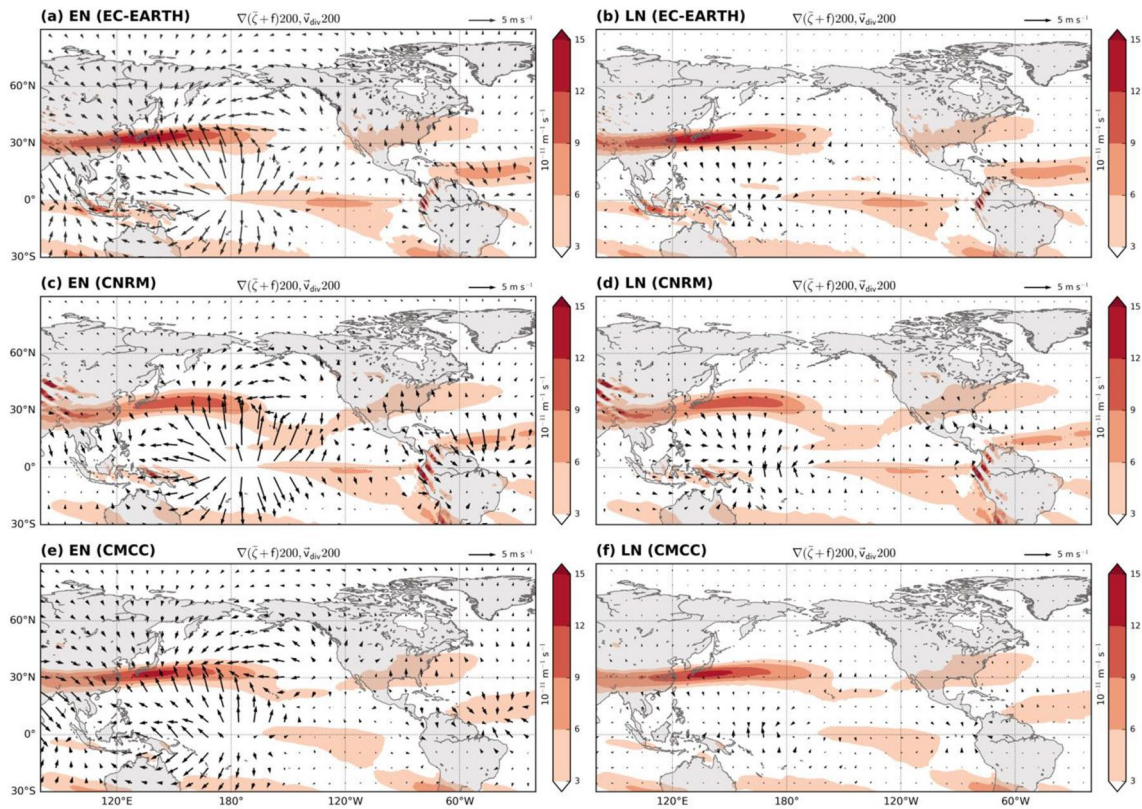


Fig. 13 Gradient of climatological vorticity in CTL (shading) and ensemble-mean 200-hPa divergent wind anomalies for (left) EN and (right) LN with respect to CTL (arrows) in JFM: EC-EARTH (top), CNRM (middle), CMCC (bottom)

Appendix 3: wavenumber-2 components of Z50

Figure 14 displays the wavenumber-2 component of EN and LN (left and middle column) in comparison with the NAO-related component.

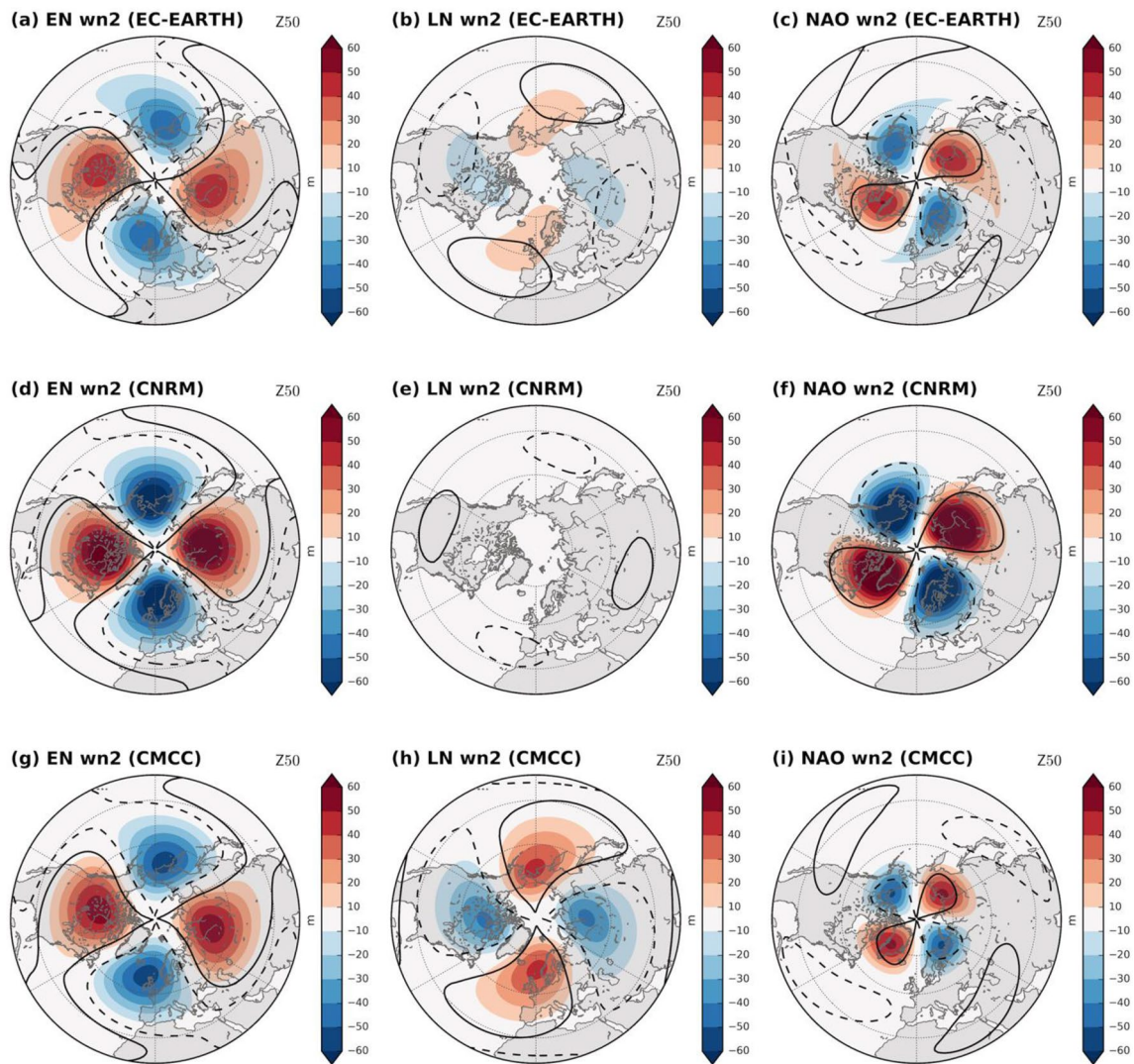


Fig. 14 Same as Fig. 9, but for the wavenumber-2 components

Appendix 4: Observational composites

Figure 15 shows JFM composites of El Niño (top left) and La Niña (top right) SLP anomalies using data from ECMWF ERA-20C (Poli et al. 2016) over 1900–2010. The composites are built according to the JFM Nino3.4-index computed

from HadISST1.1, with El Niño (La Niña) years identified when +1 (– 1) standard deviation is exceeded (18 EN and 19 LN years). The bottom panels display the symmetric (left) and asymmetric (right) components of the response.

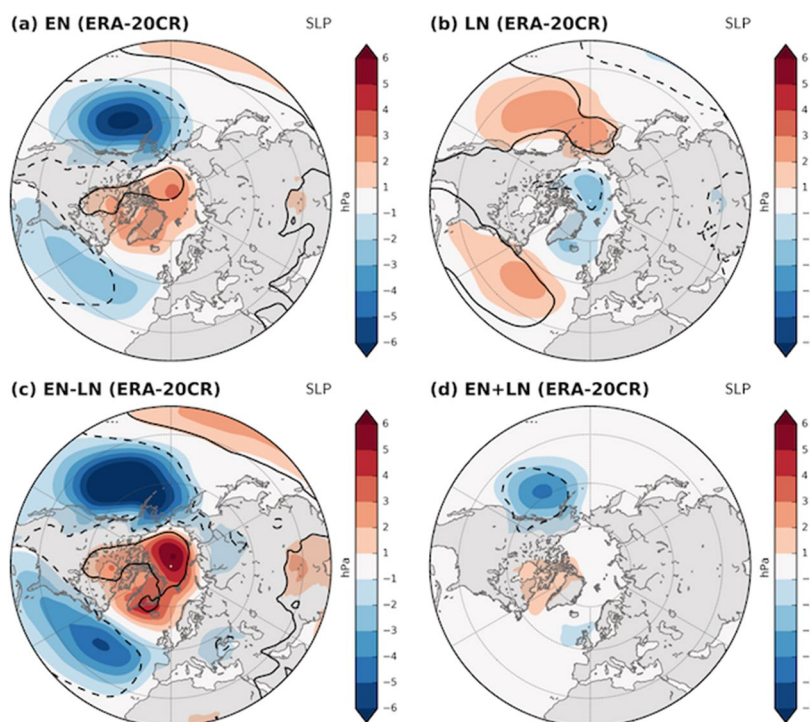


Fig. 15 Top: JFM composites of **a** El Niño **b** La Niña **c** El Niño+La Niña and **d** El Niño+La Niña anomalies using SLP data from ECMWF ERA-20C (Poli et al. 2016) over 1900–2010. Black con-

tours (solid for positive, dashed for negative anomalies) indicate statistically significant areas at the 95% confidence level

References

- Alexander MA, Bladé I, Newman M, Lanzante JR, Lau N-C et al (2002) The atmospheric bridge: the influence of ENSO teleconnections on air–sea interaction over the global oceans. *J Clim* 15:2205–2231. [https://doi.org/10.1175/1520-0442\(2002\)015,2205:TABTI O.2.0.CO;2](https://doi.org/10.1175/1520-0442(2002)015,2205:TABTI O.2.0.CO;2)
- Ambrizzi T, Hoskins BJ (1997) Stationary Rossby-wave propagation in a baroclinic atmosphere. *Q J R Meteorol Soc* 123:919–928. <https://doi.org/10.1002/qj.49712354007>
- Ayazgüena B, Ineson S, Dunstone NJ, Baldwin MP, Scaife AA (2018) Intraseasonal Effects of El Niño–Southern Oscillation on North Atlantic Climate. *J Clim* 31:8861–8873. <https://doi.org/10.1175/JCLI-D-18-0097.1>
- Back LE, Bretherton CS (2009) On the relationship between SST gradients, boundary layer winds, and convergence over the tropical oceans. *J Clim* 22:4182–4196. <https://doi.org/10.1175/2009JCLI2392.1>
- Bell CJ, Gray LJ, Charlton-Perez AJ, Joshi MM, Scaife AA (2009) Stratospheric communication of El Niño teleconnections to European winter. *J Clim* 22:4083–4096. <https://doi.org/10.1175/2009JCLI2717.1>
- Blackmon ML (1976) A climatological spectral study of the 500 mb geopotential height of the Northern hemisphere. *J Atmos Sci* 33:1607–1623. [https://doi.org/10.1175/1520-0469\(1976\)033<1607:ACSSOT>2.0.CO;2](https://doi.org/10.1175/1520-0469(1976)033<1607:ACSSOT>2.0.CO;2)
- Bladé I, Newman M, Alexander MA, Scott JD (2008) The late fall extratropical response to ENSO: sensitivity to coupling and convection in the Tropical West Pacific. *J Clim* 21:6101–6118. <https://doi.org/10.1175/2008JCLI1612.1>
- Branstator G (2002) Circumglobal teleconnections, the jet stream waveguide, and the North Atlantic Oscillation. *J Clim* 15:1893–1910. [https://doi.org/10.1175/15200442\(2002\)015,1893:CTTJS W.2.0.CO;2](https://doi.org/10.1175/15200442(2002)015,1893:CTTJS W.2.0.CO;2)
- Brönnimann S (2007) Impact of El Niño–Southern Oscillation on European climate. *Rev Geophys* 45:RG3003. <https://doi.org/10.1029/2006RG000199>
- Burgers G, Stephenson DB (1999) The “normality” of el niño. *Geophys Res Lett* 26(8):1027–1030. <https://doi.org/10.1029/1999GL900161>
- Butler AH, Polvani LM, Deser C (2014) Separating the stratospheric and tropospheric pathways of El Niño–Southern Oscillation teleconnections. *Environ Res Lett* 9:024014. <https://doi.org/10.1088/1748-9326/9/2/024014>
- Cagnazzo C, Manzini E (2009) Impact of the stratosphere on the winter tropospheric teleconnections between ENSO and the North Atlantic and European Region. *J Clim* 22:1223–1238. <https://doi.org/10.1175/2008JCLI2549.1>
- Capotondi A, Wittenberg AT, Newman M, Di Lorenzo E, Yu J-Y et al (2015) Understanding ENSO diversity. *Bull Am Meteorol Soc* 96:921–938. <https://doi.org/10.1175/BAMS-D-13-00117.1>
- Chang EK, Fu Y (2002) Interdecadal variations in Northern Hemisphere winter storm track intensity. *J Clim* 15:642–658. [https://doi.org/10.1175/1520-0442\(2002\)015,0642:IVINHW.2.0.CO;2](https://doi.org/10.1175/1520-0442(2002)015,0642:IVINHW.2.0.CO;2)
- Davini P, von Hardenberg J, Corti S, Christensen HM, Juricke S et al (2017) Climate SPHINX: evaluating the impact of resolution and stochastic physics parameterisations in the EC-Earth global climate model. *Geosci Model Dev* 10:1383–1402. <https://doi.org/10.5194/gmd-10-1383-2017>
- Deser C, Simpson IR, McKinnon KA, Phillips AS (2017) The Northern hemisphere extratropical atmospheric circulation response to

- ENSO: how well do we know it and how do we evaluate models accordingly? *J Clim* 30:5059–5082. <https://doi.org/10.1175/JCLI-D-16-0844.1>
- DeWeaver E, Nigam S (2002) Linearity in ENSO's atmospheric response. *J Clim* 15:2446–2461. [https://doi.org/10.1175/1520-0442\(2002\)015,2446:LIESAR.2.0.CO;2](https://doi.org/10.1175/1520-0442(2002)015,2446:LIESAR.2.0.CO;2)
- Domeisen DI, Garfinkel CI, Butler AH (2019) The teleconnection of El Niño Southern Oscillation to the stratosphere. *Rev Geophys* 57:5–47. <https://doi.org/10.1029/2018RG000596>
- García-Serrano J, Cassou C, Douville H, Giannini A, Doblas-Reyes FJ (2017) Revisiting the ENSO teleconnection to the tropical North Atlantic. *J Clim* 30:6945–6957. <https://doi.org/10.1175/JCLI-D-16-0641.1>
- García-Serrano J, Rodríguez-Fonseca B, Bladé I, Zurita-Gotor P, de la Cámara A (2011) Rotational atmospheric circulation during North Atlantic-European winter: the influence of ENSO. *Clim Dyn* 37:1727–1743. <https://doi.org/10.1007/s00382-010-0968-y>
- Garfinkel CI, Weinberger I, White IP, Oman LD, Aquila V et al (2019) The salience of nonlinearities in the boreal winter response to ENSO: North Pacific and North America. *Clim Dyn* 52:4429–4446. <https://doi.org/10.1007/s00382-018-4386-x>
- Gill AE (1980) Some simple solutions for heat-induced tropical circulation. *Q J R Meteorol Soc* 106:447–462. <https://doi.org/10.1002/qj.49710644905>
- Graham NE, Barnett TP (1987) Sea surface temperature, surface wind divergence, and convection over tropical oceans. *Science* 238:657–659. <https://doi.org/10.1126/science.238.4827.657>
- Gouirand I, Moron V, Zorita E (2007) Teleconnections between ENSO and North Atlantic in an ECHO-G simulation of the 1000–1990. *Geophys Res Lett* 34:L06705. doi:<https://doi.org/10.1029/2006GL028852>
- Haarsma RJ, Acosta M, Bakhshi R, Bretonnière P-A, Caron L-P et al (2020) HighResMIP versions of EC-EARTH: EC-Earth3P and EC-Earth3P-HR. Description, model computational performance and basic validation. *Geosci Model Dev*. <https://doi.org/10.5194/gmd-2019-350>
- Hardiman SC, Dunstone NJ, Scaife AA, Smith DM, Ineson S et al (2019) The impact of strong El Niño and La Niña events on the North Atlantic. *Geophys Res Lett* 46:2874–2883. <https://doi.org/10.1029/2018GL081776>
- Held IM, Ting M, Wang H (2002) Northern winter stationary waves: theory and modeling. *J Clim* 15:2125–2144. [https://doi.org/10.1175/1520-0442\(2002\)015<2125:NWSWT A>&t.2.0.CO;2](https://doi.org/10.1175/1520-0442(2002)015<2125:NWSWT A>&t.2.0.CO;2)
- Hitchcock P, Simpson IR (2014) The downward influence of stratospheric sudden warmings. *J Atmos Sci* 71:3856–3876. <https://doi.org/10.1175/JAS-D-14-0012.1>
- Hoerling MP, Kumar A, Xu T (2001) Robustness of the nonlinear climate response to ENSO's extreme phases. *J Clim* 14:1277–1293. [https://doi.org/10.1175/1520-0442\(2001\)014<1277:ROTNC R>2.0.CO;2](https://doi.org/10.1175/1520-0442(2001)014<1277:ROTNC R>2.0.CO;2)
- Hoerling MP, Kumar A, Zhong M (1997) El Niño, La Niña, and the nonlinearity of their teleconnections. *J Clim* 10:1769–1786. [https://doi.org/10.1175/1520-0442\(1997\)010<1769:ENOLN A>2.0.CO;2](https://doi.org/10.1175/1520-0442(1997)010<1769:ENOLN A>2.0.CO;2)
- Horel JD, Wallace JM (1981) Planetary-scale atmospheric phenomena associated with the Southern oscillation. *Mon Weather Rev* 109:813–829. [https://doi.org/10.1175/1520-0493\(1981\)109<0813:PSAPAW>2.0.CO;2](https://doi.org/10.1175/1520-0493(1981)109<0813:PSAPAW>2.0.CO;2)
- Hoskins BJ, James LN, White GH (1983) The shape, propagation and mean-flow interaction of large-scale weather systems. *J Atmos Sci* 40:1595–1612. [https://doi.org/10.1175/1520-0469\(1983\)040<595:TSPAMF>2.0.CO;2](https://doi.org/10.1175/1520-0469(1983)040<595:TSPAMF>2.0.CO;2)
- Hoskins BJ, Karoly DJ (1981) The steady linear response of a spherical atmosphere to thermal and orographic forcing. *J Atmos Sci* 38:1179–1196. [https://doi.org/10.1175/1520-0469\(1981\)038<1179:TSLROA>2.0.CO;2](https://doi.org/10.1175/1520-0469(1981)038<1179:TSLROA>2.0.CO;2)
- Ineson S, Scaife AA (2009) The role of the stratosphere in the European climate response to El Niño. *Nat Geosci* 2:32–36. <https://doi.org/10.1038/ngeo381>
- Jiménez-Esteve B, Domeisen DI (2018) The Tropospheric Pathway of the ENSO–North Atlantic Teleconnection. *Geophys Res Lett* 46:4563–4584. <https://doi.org/10.1175/JCLI-D-17-0716.1>
- Jiménez-Esteve B, Domeisen DI (2019) Nonlinearity in the North Pacific atmospheric response to a linear ENSO forcing. *Geophys Res Lett* 46:2271–2281. <https://doi.org/10.1029/2018GL081226>
- Jin F, Hoskins BJ (1995) The direct response to tropical heating in a baroclinic atmosphere. *J Atmos Sci* 52:307–319. [https://doi.org/10.1175/1520-0469\(1995\)052<0307:TDRTH>2.0.CO;2](https://doi.org/10.1175/1520-0469(1995)052<0307:TDRTH>2.0.CO;2)
- Kidston J, Scaife AA, Hardiman SC, Mitchell DM, Butchart N et al (2015) Stratospheric influence on tropospheric jet streams, storm tracks and surface weather. *Nat Geosci* 8:433–440. <https://doi.org/10.1038/ngeo2424>
- King MP, Hecceg-Bulić I, Bladé I, García-Serrano J, Keenlyside N et al (2018) Importance of late fall ENSO teleconnection in the Euro-Atlantic sector. *Bull Am Meteorol Soc* 99:1337–1343. <https://doi.org/10.1175/BAMS-D-17-0020.1>
- Lee S, Wang C, Mapes BE (2009) A simple atmospheric model of the local and teleconnection responses to tropical heating anomalies. *J Clim* 22:272–284. <https://doi.org/10.1175/2008JCLI2303.1>
- Lau N-C (1988) Variability of the observed midlatitude storm tracks in relation to low-frequency changes in the circulation pattern. *J Atmos Sci* 45:2718–2743. [https://doi.org/10.1175/1520-0469\(1988\)045<2718:VOTOMS>2.0.CO;2](https://doi.org/10.1175/1520-0469(1988)045<2718:VOTOMS>2.0.CO;2)
- Lindzen RS, Nigam S (1987) On the role of sea surface temperature gradients in forcing low-level winds and convergence in the tropics. *J Atmos Sci* 44:2418–2436. [https://doi.org/10.1175/1520-0469\(1987\)044<2418:OTROSS>2.0.CO;2](https://doi.org/10.1175/1520-0469(1987)044<2418:OTROSS>2.0.CO;2)
- Matsuno T (1966) Quasi-geostrophic motions in the equatorial area. *J Meteorol Soc Jpn* 44:25–43. https://doi.org/10.2151/jmsj1965.44.1_25
- Mezzina B, García-Serrano J, Bladé I, Kucharski F (2020) Dynamics of the ENSO teleconnection and NAO variability in the North Atlantic–European late winter. *J Clim* 33:907–923. <https://doi.org/10.1175/JCLI-D-19-0192.1>
- Moron V, Gouirand I (2003) Seasonal modulation of the El Niño–Southern Oscillation relationship with sea level pressure anomalies over the North Atlantic in October–March (1873–1996). *Int J Climatol* 23:143–155. <https://doi.org/10.1002/joc.868>
- Numaguti A, Hayashi Y-Y (1991) Behavior of cumulus activity and the structures of circulations in an “Aqua Planet” model. *J Meteorol Soc Jpn* 69:563–579. https://doi.org/10.2151/jmsj1965.69.5_563
- Poli P, Hersbach H, Dee DP, Berrisford P, Simmons AJ et al (2016) ERA-20C: an atmospheric reanalysis of the twentieth century. *J Clim* 29:4083–4097. <https://doi.org/10.1175/JCLI-D-15-0556.1>
- Pozo-Vázquez D, Esteban-Parra MJ, Rodrigo FS, Castro-Díez Y (2001) The association between ENSO and winter atmospheric circulation and temperature in the North Atlantic Region. *J Clim* 14:3408–3420. [https://doi.org/10.1175/1520-0442\(2001\)014<3408:TABEAW>2.0.CO;2](https://doi.org/10.1175/1520-0442(2001)014<3408:TABEAW>2.0.CO;2)
- Qin J, Robinson WA (1993) On the Rossby wave source and the steady linear response to tropical forcing. *J Atmos Sci* 50:1819–1823. [https://doi.org/10.1175/1520-0469\(1993\)050<1819:OTRWS A>2.0.CO;2](https://doi.org/10.1175/1520-0469(1993)050<1819:OTRWS A>2.0.CO;2)
- Rao J, Ren R (2016a) Asymmetry and nonlinearity of the influence of ENSO on the northern winter stratosphere: 1. Observations. *J Geophys Res Atmos* 121:9000–9016. doi:<https://doi.org/10.1002/2015JD024520>
- Rao J, Ren R (2016b) Asymmetry and nonlinearity of the influence of ENSO on the northern winter stratosphere: 2. Model study with

- WACCM. *J Geophys Res Atmos* 121:9017–9032. doi:<https://doi.org/10.1002/2015JD024521>
- Roehrig R, Beau I, Saint-Martin D, Alias A, Decharme B et al (2020) The CNRM global atmosphere model ARPEGE-Climat 6.3: description and evaluation. *J Adv Model Earth Syst*
- Sanna A, Borrelli A, Athanasiadis P, Matera S, Storto A et al (2017) CMCC-SPS3: the CMCC seasonal prediction system 3. CMCC Tech Rep RP0285:61
- Sardeshmukh PD, Compo GP, Penland C (2000) Changes of probability associated with El Niño. *J. Clim* 13:4268–4286. [https://doi.org/10.1175/1520-0442\(2000\)013<4268:COPAWE>2.0.CO;2](https://doi.org/10.1175/1520-0442(2000)013<4268:COPAWE>2.0.CO;2)
- Sardeshmukh PD, Hoskins BJ (1987) On the derivation of the divergent flow from the rotational flow: the χ problem. *Q J R Meteorol Soc* 113:339–360. <https://doi.org/10.1002/qj.49711347519>
- Sardeshmukh PD, Hoskins BJ (1988) The generation of global rotational flow by steady idealized tropical divergence. *J Atmos Sci* 45:1228–1251. [https://doi.org/10.1175/1520-0469\(1988\)045<1228:TGOGRF>2.0.CO;2](https://doi.org/10.1175/1520-0469(1988)045<1228:TGOGRF>2.0.CO;2)
- Taguchi M, Hartmann DL (2006) Increased occurrence of stratospheric sudden warmings during El Niño as simulated by WACCM. *J Clim* 19:324–332. <https://doi.org/10.1175/JCLI3655.1>
- Timmermann A, An S, Kug J, Jin F-F, Cai W et al (2018) (2018) El Niño-Southern Oscillation complexity. *Nature* 559:535–545. <https://doi.org/10.1038/s41586-018-0252-6>
- Ting M (1996) Steady linear response to tropical heating in barotropic and baroclinic models. *J Atmos Sci* 53:1698–1709. [https://doi.org/10.1175/1520-0469\(1996\)053<1698:SLRTTH>2.0.CO;2](https://doi.org/10.1175/1520-0469(1996)053<1698:SLRTTH>2.0.CO;2)
- Titchner HA, Rayner NA (2014) The Met Office Hadley Centre sea ice and sea surface temperature data set, version 2: 1. Sea ice concentrations. *J Geophys Res Atmos* 119:2864–2889. <https://doi.org/10.1002/2013JD020316>
- Toniazzo T, Scaife AA (2006) The influence of ENSO on winter North Atlantic climate. *Geophys Res Lett* 33:L24704. doi:<https://doi.org/10.1029/2006GL027881>
- Trascasa-Castro P, Maycock AC, Scott Yiu YY, Fletcher JK (2019) On the linearity of the stratospheric and Euro-Atlantic sector response to ENSO. *J Clim* 32:6607–6626. <https://doi.org/10.1175/JCLI-D-18-0746.1>
- Trenberth KE (1986) An assessment of the impact of transient eddies on the zonal flow during a blocking episode using localized Eliassen-Palm flux diagnostics. *J Atmos Sci* 43:2070–2087. [https://doi.org/10.1175/1520-0469\(1986\)043<2070:AAOTIO>2.0.CO;2](https://doi.org/10.1175/1520-0469(1986)043<2070:AAOTIO>2.0.CO;2)
- Trenberth KE, Branstator GW, Karoly D, Kumar A, Lau N-C, Ropelewski C (1998) Progress during TOGA in understanding and modeling global teleconnections associated with tropical sea surface temperatures. *J Geophys Res* 103(C7):14291–14324. <https://doi.org/10.1029/97JC01444>
- Voltaire A, Saint-Martin D, Sénési S, Decharme B, Alias A et al (2019) Evaluation of CMIP6 DECK experiments with CNRM-CM6-1. *J Adv Model Earth Syst* 11:2177–2213. <https://doi.org/10.1029/2019MS001683>
- Wallace JM, Lim G, Blackmon ML (1988) Relationship between cyclone tracks, anticyclone tracks and baroclinic waveguides. *J Atmos Sci* 45:439–462. [https://doi.org/10.1175/1520-0469\(1988\)045<0439:RBCTAT>2.0.CO;2](https://doi.org/10.1175/1520-0469(1988)045<0439:RBCTAT>2.0.CO;2)
- Wang C (2005) ENSO, Atlantic climate variability and the Walker and Hadley circulations. In: Diaz HF, Bradley RS (eds) *The Hadley Circulation: present, past and future*. Kluwer Academic Publishers, The Netherlands, pp 173–202
- Weinberger I, Garfinkel CI, White IP, Oman LD (2019) The salience of nonlinearities in the boreal winter response to ENSO: Arctic stratosphere and Europe. *Clim Dyn* 53:4591–4610. <https://doi.org/10.1007/s00382-019-04805-1>
- Zhang W, Wang Z, Stuecker MF, Turner AG, Jin F-F et al (2019) Impact of ENSO longitudinal position on teleconnections to the NAO. *Clim Dyn* 52:257–274. <https://doi.org/10.1007/s00382-018-4135-1>

Publisher's Note Springer Nature remains neutral with regard to jurisdictional claims in published maps and institutional affiliations.